

MECHANICAL PROPERTIES COMPARISON OF STRUT-BASED AND TPMS
LATTICE STRUCTURES PRODUCED BY EBM

A THESIS SUBMITTED TO
THE GRADUATE SCHOOL OF NATURAL AND APPLIED SCIENCES
OF
MIDDLE EAST TECHNICAL UNIVERSITY

BY

BARIŞ SOKOLLU

IN PARTIAL FULFILLMENT OF THE REQUIREMENTS
FOR
THE DEGREE OF MASTER OF SCIENCE
IN
MECHANICAL ENGINEERING

APRIL 2022

Approval of the thesis:

**MECHANICAL PROPERTIES COMPARISON OF STRUT-BASED AND
TPMS LATTICE STRUCTURES PRODUCED BY EBM**

submitted by **BARIŞ SOKOLLU** in partial fulfillment of the requirements for the
degree of **Master of Science** in **Mechanical Engineering**, **Middle East Technical
University** by,

Prof. Dr. Halil Kalıpçılar
Dean, Graduate School of **Natural and Applied Sciences**

Prof. Dr. M. A. Sahir Arıkan
Head of the Department, **Mechanical Engineering**

Prof. Dr. Erhan İlhan Konukseven
Supervisor, **Mechanical Engineering, METU**

Dr. Orhan Gülcan
Co-Supervisor, **Additive Design, GE Aviation**

Examining Committee Members:

Assoc. Prof. Kıvanç Azgın
Mechanical Engineering, METU

Prof. Dr. Erhan İlhan Konukseven
Mechanical Engineering, METU

Prof. Dr. Oğuzhan Yılmaz
Mechanical Engineering, Gazi University

Assoc. Prof. Ulaş Yaman
Mechanical Engineering, METU

Assoc. Prof. Ender Yıldırım
Mechanical Engineering, METU

Date: 28.04.2022

I hereby declare that all information in this document has been obtained and presented in accordance with academic rules and ethical conduct. I also declare that, as required by these rules and conduct, I have fully cited and referenced all material and results that are not original to this work.

Name, Surname : Barış Sokollu

Signature:

ABSTRACT

MECHANICAL PROPERTIES COMPARISON OF STRUT-BASED AND TPMS LATTICE STRUCTURES PRODUCED BY EBM

Sokollu, Barış
Master of Science, Mechanical Engineering
Supervisor: Prof. Dr. Erhan İlhan Konukseven
Co-Supervisor: Dr. Orhan Gülcan

April 2022, 86 pages

Additive manufacturing is a relatively old but rapidly emerging innovative technology that enables various shapes and designs to be realized which are almost not possible with conventional manufacturing. Lattice structures are one of the most unique applications of utilizing additive manufacturing technology due to weight-to-strength ratios they offer, high impact absorption capabilities, and difficult to produce with conventional approaches. Studies in the literature are mainly focusing on the strut-based crystal-like structures i.e., Body-Centered Cubic (BCC) and Face-Centered Cubic (FCC) while fewer studies examine the Triply Periodic Minimal Surface (TPMS) topologies. Although there are several works showing the mechanical properties of these topologies individually, there is a lack of comparative study in the literature. In this thesis work, comparative investigation of mechanical responses of five different lattice topologies which are BCC, FCC, Gyroid, Primitive, and Diamond under tension and compression loads is aimed. Scope of the thesis is specified as powder removal study, production of test samples made by Ti6Al4V, Scanning Electron Microscope (SEM) imaging prior to experiments, conducting tension and compression testing considering available standards, comparison of compression results with Gibson-Ashby theoretical model, investigation of

microstructures from fracture surfaces, and finite element analysis (FEA) verification by the test results.

Keywords: Additive Manufacturing, Lattice Structures, Triply Periodic Minimal Surfaces, Electron Beam Melting, Ti6Al4V

ÖZ

EBM İLE ÜRETİLEN DİKME TABANLI VE TPMS KAFES YAPILARIN MEKANİK ÖZELLİKLERİNİN KARŞILAŞTIRILMASI

Sokollu, Barış
Yüksek Lisans, Makina Mühendisliği
Tez Yöneticisi: Prof. Dr. Erhan İlhan Konukseven
Ortak Tez Yöneticisi: Dr. Orhan Gülcan

Nisan 2022, 86 sayfa

Eklemeli imalat, konvansiyonel metotlarla üretilmesi neredeyse imkansız olan şekil ve tasarımların üretilmesine olanak sağlayan, eski sayılabilecek ancak son yıllarda çok hızlı gelişme gösteren inovatif bir teknolojidir. Kafes yapılar ise sundukları ağırlık-dayanım oranları, yüksek darbe sönümleme kabiliyetleri ve geleneksel yaklaşımlarla üretilmelerinin zor olması nedeniyle eklemeli imalat teknolojisinden yararlanmanın en eşsiz uygulamalarından biridir. Literatürdeki çalışmalar çoğunluk olarak Hacim Merkezli Kübik (HMK) ya da Yüzey Merkezli Kübik (YMK) gibi kristal yapı benzetimli dikme tabanlı yapılara odaklanırken, daha az bir kısmı ise Üçlü Yönlü Periyodik Minimal Yüzey (ÜYPMY) topolojilerini incelemektedir. Bu çalışmaların çoğunda kafes topolojilerinin mekanik özellikleri kendi içlerinde değerlendirilse de, literatürde farklı topolojilerin mekanik özelliklerini karşılaştırmalı şekilde ele alan çalışma sayısının azlığı dikkat çekmektedir. Bu tez çalışmasında beş farklı kafes topolojisinin (HMK, YMK, Gyroid, Primitive ve Gyroid) çekme ve basma yükleri altındaki mekanik özelliklerinin karşılaştırmalı şekilde incelenmesi amaçlanmıştır. Toz uzaklaştırma çalışması, Ti6Al4V kullanılarak deney numuneleri üretimi, numunelerin test öncesi taramalı elektron mikroskobu görüntülemesinin yapılması, mevcut standartlar dikkate alınarak çekme ve basma deneylerinin yapılması, basma testi sonuçlarının Gibson-Ashby teorik

modeli ile karşılaştırılması, test sonrası kırılma yüzeylerinden mikroyapıların incelenmesi ve deney sonuçlarının sonlu elemanlar analizleri ile doğrulanması tezin kapsamını oluşturmaktadır.

Anahtar Kelimeler: Eklemeli İmalat, Kafes Yapılar, Üçlü Periyodik Minimal Yüzeyler, Elektron Işınıyla Ergitme, Ti6Al4V

To my beloved

ACKNOWLEDGMENTS

I would like to express my deepest gratitude to my supervisor Prof. Dr. Erhan İlhan Konukseven, who made this thesis work possible and guided me throughout the years of study. I am also grateful to him for being patient with the tough times while dealing with both my job and thesis together.

I would also like to thank my co-supervisor Dr. Orhan Gülcan, who encouraged me and enlighten my path with his vision through this work.

I would like to thank my company Turkish Aerospace for the opportunities they provided me at every stage of my thesis, and my colleagues who contributed to this work by making these opportunities a reality.

I would also like to thank my whole family, especially my parents Levent and Birsen Sokollu, who raised me and never lost their faith in me.

I owe my special thanks to my lovely wife Begüm Sokollu for standing by me all the time and being the embodiment of perseverance and dedication in my life.

TABLE OF CONTENTS

ABSTRACT.....	v
ÖZ	vii
ACKNOWLEDGMENTS	x
TABLE OF CONTENTS	xi
LIST OF TABLES	xiii
LIST OF FIGURES.....	xiv
LIST OF ABBREVIATIONS	xviii
CHAPTERS	
1 INTRODUCTION	1
1.1 Development of Additive Manufacturing	1
1.2 Lattice Structures in the Era of Additive Manufacturing.....	3
1.3 Motivation and Scope of the Study	5
2 LITERATURE REVIEW	7
2.1 Lattice Structures - Overview.....	7
2.2 Strut-based Lattice Structures	9
2.2.1 Body-Centered Cubic (BCC).....	9
2.2.2 Face-Centered Cubic (FCC)	9
2.3 Triply Periodic Minimal Surface (TPMS) Lattice Structures	10
2.3.1 Schwarz Primitive (Primitive) and Schwarz Diamond (Diamond)	11
2.3.2 Schoen's Gyroid	11
2.4 Mechanical Properties of Metallic Lattice Structures under Compression and Tension Loads	12
3 METHOD AND WORKFLOW	21

3.1	Electron Beam Melting (EBM).....	21
3.2	Modelling of Lattice Structures	24
3.2.1	Determination of Overall Test Geometries	26
3.2.2	Unit Cell Parameters.....	29
3.2.3	Manufacturing Constraints	30
3.3	Manufacturing Stage.....	36
3.3.1	Production of Demo Parts	37
3.3.2	Production of Test Samples.....	39
3.4	Experimental Study.....	42
4	RESULTS.....	43
4.1	Scanning Electron Microscope (SEM) Investigation	43
4.2	Comparison of Test Results	46
4.2.1	Tensile Test	46
4.2.2	Compression Test	49
4.2.3	Theoretical Model	53
4.3	Comparison of FEA and Test Results.....	56
4.4	Microstructure Investigation.....	69
5	CONCLUSION AND FUTURE WORK.....	73
	REFERENCES	77

LIST OF TABLES

TABLES

Table 2.1 Implicit iso-surface equations ($U = 0$) for TPMS lattices [24].	11
Table 3.1 Technical specifications of Arcam EBM Q20plus [52].	23
Table 3.2 Dimensions of tensile test specimen (all values are in mm).	27
Table 3.3 Melt theme process parameters for Arcam EBM Q20plus.	32
Table 3.4 Strut diameter and wall thickness values for lattice types with two different parameter sets (all values are in mm).	35
Table 3.5 Chemical composition of Ti6Al4V powder provided by supplier.	37
Table 4.1 Comparison of diameter and wall thicknesses.	45
Table 4.2 Sample cross-sections for each topology used in tensile tests.	47
Table 4.3 Mechanical properties of lattices obtained from tensile tests.	49
Table 4.4 Sample cross-sections for each topology used in compression tests.	50
Table 4.5 Mechanical properties of lattices obtained from compression tests.	51
Table 4.6 Mechanical property formulations of lattices based on relative densities and response types.	54
Table 4.7 Gibson-Ashby coefficients derived from experimental results.	56

LIST OF FIGURES

FIGURES

Figure 1.1. AM technologies along with materials they use.	2
Figure 1.2. Schematic view for one of the PBF systems: Selective Laser Sintering [5].	3
Figure 2.1. Classification of lattice structures: a) disordered (random) lattices b) periodic lattices c) pseudo-periodic (conformal) lattices [17].	8
Figure 2.2. Unit cell representations of strut-based lattice structures: a) BCC b) FCC.	10
Figure 2.3. Unit cell representations of sheet TPMS lattices: a) Primitive b) Diamond c) Gyroid.	12
Figure 2.4. Stress-strain relation of stretch-dominated and bending-dominated lattice structures under compressive loads [15].	13
Figure 2.5. Diagonal shear failure mode in DG lattice with unit cell size of 3 mm [34].	14
Figure 2.6. Tensile tests results of Neovius and IWP lattices with varying cell sizes [39].	15
Figure 2.7. Tensile response of gyroid structures produced with different process parameters: a) Melt theme, b) Wafer theme [46].	17
Figure 2.8. Comparison of strain-stress curves obtained from FEA and test results of four different lattices: a) primitive b) diamond c) gyroid d) BCC [49].	18
Figure 3.1. Arcam EBM Q20plus machine on the left and the layout of EBM system is on the right [52].	23
Figure 3.2. Volume Lattice building block and Walled TPMS building block.	25
Figure 3.3. Tensile test specimen geometry to be used [58].	27
Figure 3.4. Comparison of the overall geometries for tensile testing.	28
Figure 3.5. Overall geometry of compression test samples.	29
Figure 3.6. Comparison of struts in diameter of 1 mm produced with “Net” theme (a) and “Melt” theme (b) where blue regions represent nominal CAD data [62]. ..	31

Figure 3.7. Section cut of a 1.5 mm strut produced with “Net” theme [62].	31
Figure 3.8. Extrapolated version of part thickness and pore size correlation for powder removal using PRS [65].	34
Figure 3.9. Pore sizes on CAD representations of alternatively designed lattices..	34
Figure 3.10. Ramp function used to grade diameter and thickness of lattices, and illustration of geometry with and without grading on FCC sample.	36
Figure 3.11. Demo production models for powder removal study.	38
Figure 3.12. Produced demo parts after PRS and manual powder removal operation.	39
Figure 3.13. Distribution of parts on the build plate.	40
Figure 3.14. Gap between stacked compression test samples and support structures.	41
Figure 3.15. Tensile test specimens after powder removal: a) FCC b) BCC c) Primitive d) Diamond e) Gyroid	41
Figure 3.16. Compression test specimens after powder removal: a) FCC b) BCC c) Primitive d) Diamond e) Gyroid.	42
Figure 3.17. Machines used in experimental study (Zwick Z250 and Instron 5985).	42
Figure 4.1. Thickness measurements on SEM images: a) FCC b) BCC c) Primitive d) Diamond e) Gyroid.	44
Figure 4.2. Detailed SEM images of production related defects.	46
Figure 4.3. Tensile behavior comparison of different lattice topologies.	48
Figure 4.4. Compressive behavior comparison of different lattice topologies.	50
Figure 4.5. Stress-strain curve showing the quasi-elastic gradient and compressive offset stress.	51
Figure 4.6. Compression test stages with 10% strain increments.	53
Figure 4.7. METTLER TOLEDO XS204 analytical balance device.	55
Figure 4.8. FEA boundary conditions of tensile test specimen with BCC.	57
Figure 4.9. FEA boundary conditions of compression test specimen with BCC. ..	57

Figure 4.10. Comparison of FEA and experimental results of FCC under tensile loading.	58
Figure 4.11. Comparison of FEA and experimental results of BCC under tensile loading.	58
Figure 4.12. Comparison of FEA and experimental results of Primitive under tensile loading.	59
Figure 4.13. Comparison of FEA and experimental results of Diamond under tensile loading.	59
Figure 4.14. Comparison of FEA and experimental results of Gyroid under tensile loading.	60
Figure 4.15. von Mises stress plot and fractured tension specimens of FCC.	61
Figure 4.16. von Mises stress plot and fractured tension specimens of BCC.	61
Figure 4.17. von Mises stress plot and fractured tension specimens of Primitive. .	62
Figure 4.18. von Mises stress plot and fractured tension specimens of Diamond. .	62
Figure 4.19. von Mises stress plot and fractured tension specimens of Gyroid.	63
Figure 4.20. Comparison of FEA and experimental results of FCC under compressive loading.	64
Figure 4.21. Comparison of FEA and experimental results of BCC under compressive loading.	64
Figure 4.22. Comparison of FEA and experimental results of Primitive under compressive loading.	65
Figure 4.23. Comparison of FEA and experimental results of Diamond under compressive loading.	65
Figure 4.24. Comparison of FEA and experimental results of Gyroid under compressive loading.	66
Figure 4.25. Displacement (left) and von Mises stress plots (right) for FCC at ~8% strain.	67
Figure 4.26. Displacement (left) and von Mises stress plots (right) for BCC at ~8% strain.	67

Figure 4.27. Displacement (left) and von Mises stress plots (right) for Primitive at ~8% strain.	68
Figure 4.28. Displacement (left) and von Mises stress plots (right) for Diamond at ~8% strain.	68
Figure 4.29. Displacement (left) and von Mises stress plots (right) for Gyroid at ~8% strain.	69
Figure 4.30. Struers CitoPress-1 Mounting Press (left) and Struers LaboForce-100 (right) machines.	70
Figure 4.31. Nikon ECLIPSE MA100 Optical Microscope.	70
Figure 4.32. Microstructures of fractured tensile test specimen portions: a) FCC b) BCC c) Primitive d) Diamond e) Gyroid.	72

LIST OF ABBREVIATIONS

ABBREVIATIONS

AM: Additive Manufacturing

BCC: Body-Centered Cubic

BJ: Binder Jetting

DOF: Degrees of Freedom

FCC: Face-Centered Cubic

FEA: Finite Element Analysis

FDM: Fused Deposition Modeling

FFF: Fused Filament Fabrication

DED: Direct Energy Deposition

MJ: Material Jetting

LOM: Laminated Object Manufacturing

PBF: Powder Bed Fusion

SD: Standard Deviation

SLA: Stereolithography

TPMS: Triply Periodic Minimal Surface

UTS: Ultimate Tensile Strength

YS: Yield Strength

CHAPTER 1

INTRODUCTION

Additive manufacturing (AM), often referred to as 3D printing or rapid prototyping, is a relatively new manufacturing method compared to traditional manufacturing technologies. However, in today's world where technological development is very rapid, this technology, which emerged in the mid-1980s, should not be described as new, because the increasing number of device manufacturers in the market and the development of existing methods have brought additive manufacturing to a highly competitive position in the industry market.

1.1 Development of Additive Manufacturing

The first additive manufacturing method in the literature is the Stereolithography (SLA) method, which was developed by Charles Hull in 1983 and whose patent was approved in 1986. In the following periods, various new methods such as fused filament fabrication, powder bed fusion and direct energy deposition have been developed, and the materials used have diversified day by day. Today, additive manufacturing has become an industry with a market share of approximately \$15 billion on average [1], which finds its place in different fields such as automotive, defense, aerospace, dental, fashion, jewelery, food, and etc. [2].

In the ISO/ASTM 52900, additive manufacturing is defined as producing parts from 3D model data by combining materials in layers, unlike other methods based on material subtraction or forming [3]. According to this standard, additive manufacturing methods are divided into seven main categories based on the diversity of processes: binder jetting (BJ), directed energy deposition (DED), material

extrusion (FDM or FFF), material jetting (MJ), powder bed fusion (PBF), sheet lamination (LOM), and vat photopolymerization (SLA). Basically, in most additive manufacturing methods, the process takes place by connecting (bonding) materials together using an energy source. This bonding can be in the form of adhesion of semi-molten filaments (FFF systems), sintering or melting of powders (PBF systems), solidification of liquid photopolymer (SLA systems), or bonding of thin sheets with heat-activated resin (LOM systems), depending on the energy source and the difference of materials used [4]. Figure 1.1 shows these seven AM methods with the material types used with.

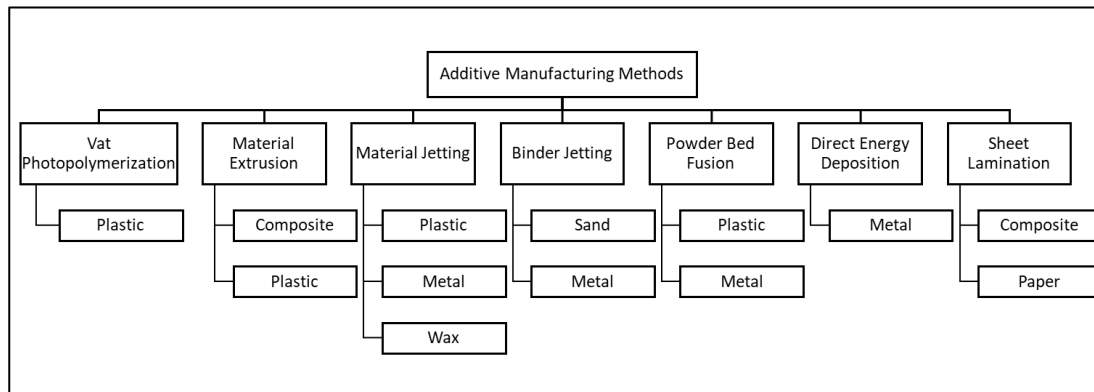


Figure 1.1. AM technologies along with materials they use.

Among these seven AM methods, PBF is commonly preferred method to produce final parts in the industry. In this method, the energy is applied by a laser or electron beam energy to melt or sinter the powdered material to form a single cross-section of a part. Once the process is done for a layer, the build platform that powders lie on is lowered and powders of the new layer is distributed by a recoater. This process continues until parts are created. The part remains in the non-melted powder pool during production with PBF systems, hence these powders act as a natural support structure to the produced geometry, reducing the need for additional support structures. After the production is completed, the non-melted powder around the part (and inside, if any) is removed, and the part is separated from the production table

by hand or with the help of a tool. The general schematic of the devices working with the PBF system is shown in Figure 1.2.

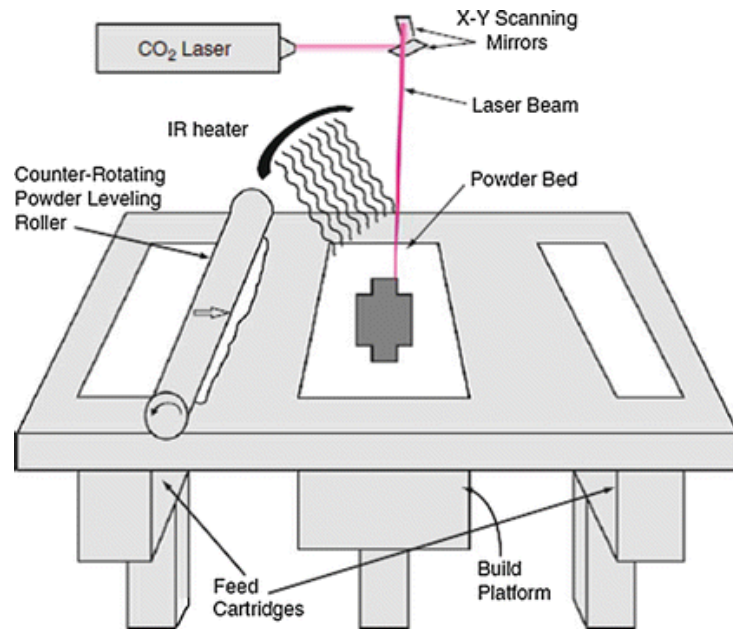


Figure 1.2. Schematic view for one of the PBF systems: Selective Laser Sintering [5].

1.2 Lattice Structures in the Era of Additive Manufacturing

The invention and widespread usage of additive manufacturing have changed the way of thinking on production. It has the capability to build a variety of designs that are almost impossible to fabricate with conventional methods. Among these, lattice structures (also known as cellular solid structures, cellular metals, cellular foam structures, porous structures or scaffold structures [6]) can be counted as one of the most complex geometrical shapes that are difficult to produce without additive manufacturing technologies.

Before additive manufacturing became widespread, lattice structures can be produced by using conventional techniques such as folding operations [7],

investment casting by using wax or polymer molds [8], or carbon fiber reinforcement methods like fiber interlacing [9]. Although it is possible to produce lattice structures with such traditional methods, it is still a costly production process in terms of mold preparation processes, additional fixture or machining preparation requirements, and the time spent to produce the final part. Thanks to the design freedom arising from the nature of AM which is a layer-by-layer manufacturing process, the production of lattice structures has become much easier than conventional methods and has gained popularity recently.

With the development of additive manufacturing and the freedom of design especially offered by PBF systems, the interest in lattice structures has increased significantly both in the academia and industry. The aerospace industry applications draw attention where weight reduction and energy absorption are needed together with high specific strength that can be satisfied by pores inside the lattice structures [10]. In fact, lattice structures are likely to replace honeycomb applications in the aviation field thanks to the complex design freedom they provide, being able to be produced as they are designed, and is designed accordingly to the load conditions in where they will be used. Lattice structures can also be used in heat exchangers due to their large surface areas [11], or as energy absorbers due to their tolerance to deformation [12]. These structures also gain importance in the biomedical field as structures that allow the bone tissue to ingrowth for successful bone regeneration. For example, Xiong et al. illustrate in their study that lattice structures with a dense core may help the bone tissue to integrate and adhere to the implant while satisfying the required compression strength [13]. These and many similar studies show that lattice structures have become interesting in several sectors thanks to the mechanical properties they offer with additive manufacturing.

1.3 Motivation and Scope of the Study

There are many studies in the literature on lattice structures, which have gained popularity with the industrial use of additive manufacturing. The main purpose of this thesis study is to contribute to the gap in the literature arising from the limited number of comparative studies of different lattice structures produced by the EBM method. In addition, with the results to be obtained from this study, it is aimed to facilitate the selection of the appropriate topology during the design phase of the lattice structures to be produced on the EBM machine, which is widely used in aviation, automotive and medical fields.

The remainder of this thesis includes the literature survey about the fundamentals of lattice structures, the procedure followed in this study to generate mechanical testing samples filled by lattices, comparison of test results with comments on SEM investigations and fracture surface analysis, and conclusion remarks based on observations from this work. Furthermore, the manufacturability and powder removal interim studies for the lattice designs to be used in the experimental specimens are also investigated individually.

CHAPTER 2

LITERATURE REVIEW

2.1 Lattice Structures - Overview

In 1997, Gibson and Ashby introduced the cellular solid structure concept that includes honeycombs, foams, and some natural materials such as wood or porous bone tissues [14]. In addition to these, lattice structures are also counted as cellular materials, but their unit cell fill type and physical/mechanical properties differ from foams and honeycombs [15]. Furthermore, studies in the literature revealed that lattices have better mechanical properties than honeycomb and foam structures [16]. In fact, since each of the carrier elements (struts, surfaces, etc.) in the unit cells of the lattices can be customized, the structure can be optimized considering the loads that it will encounter during its service life. That makes the lattice structures superior to foam and honeycombs.

A full classification has not yet been established, as lattice structures are composed of interconnected elements that repeat in space, and their arrangement can vary depending on the individual who creates the structure. Nevertheless, there have been researchers who made classification studies for these structures in the literature. To give an example, as can be seen in Figure 2.1, Dong et al. categorize the lattice structures into three groups depending on their degree of order of the lattice frame [17]. According to their study, lattice structures can be grouped under three subsections as disordered (random) lattices, periodic lattices, and pseudo-periodic (conformal) lattices.

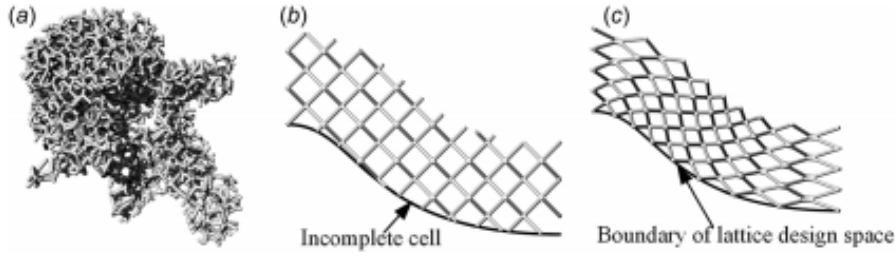


Figure 2.1. Classification of lattice structures: a) disordered (random) lattices b) periodic lattices c) pseudo-periodic (conformal) lattices [17].

Considering the predictability of their mechanical responses under various load conditions and the reproducibility, it can be said that periodic and pseudo-periodic lattice structures are more common in practice. Furthermore, by satisfying the integration between adjacent contour surfaces with unit cells, the whole structure gets stiffer in the conformal lattices. When the issue is the design of the lattice structure, the design of the unit cells, and the repetitive pattern should be understood since lattice structures consist of these patterns including the same or similar unit cells. In this project, members from two different lattice families, namely strut-based and triply periodic minimal surface lattices, having fixed repetitive patterns and conformal boundaries to be investigated.

Tao and Leo state that three types of methods for unit cell design can be used which are topology optimization, basic Boolean operations of primitive geometries, and finally using mathematically expressed implicit surfaces method [18]. The method of mathematical expressions provides convenience for the designer to interfere with the pattern of the lattice structure, to create local density differences, or even to differentiate the unit cell structure by simply modifying the equations. The commercial software selected for the designing of the test samples to be used in the later parts of the study is also based on the mathematical expression approach.

2.2 Strut-based Lattice Structures

It has been previously explained that the smallest structure that forms the repeating lattice pattern is called the unit cell, and these unit cells are formed by different topologies. Several topologies exist in the literature, but BCC, FCC, octet-truss, and rhombic-dodecahedron structures are the most studied types among them. In this study, the scope is limited to BCC and FCC topologies as strut-based lattices.

The names of BCC and FCC basically come from the analogy of crystal structures in similar forms. A crystal structure is the spatial arrangement of atoms, ions, and molecules, and this crystal structure consists of repeating unit cells in which the atoms are positioned in a certain way [19].

2.2.1 Body-Centered Cubic (BCC)

In the BCC, atoms are arranged so that one-eighth of the atoms settle on each corner of the cell while another atom is positioned in the center of the unit cell. In this structure, atoms come into contact only on the volumetric diagonal of the unit cell. This contact line indicates the unit cell struts, and atomic centers show the intersection points (nodes).

2.2.2 Face-Centered Cubic (FCC)

In FCC, atoms are positioned such as they are one-eighth in size at the corner of each surface of the unit cell, and half of an atom in the center of the same surface. Contact lines diagonally lie on each face of the cell so that corresponding lattice struts also have the same orientation.

Figure 2.2 shows the unit cell illustrations of above-mentioned strut-based lattices

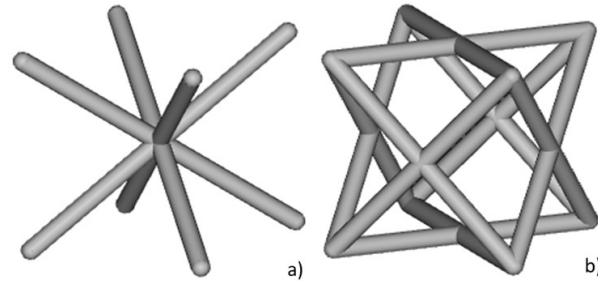


Figure 2.2. Unit cell representations of strut-based lattice structures: a) BCC b) FCC.

2.3 Triply Periodic Minimal Surface (TPMS) Lattice Structures

TPMS, as its name implies, is a structure that periodically repeating in three dimensions while minimizing surface area within given boundaries. The term minimal surface defines surfaces where the mean curvature is equal to zero at every point, so the name TPMS is derived from the minimal properties of these geometries in three different directions [20]. TPMS geometries offer less stress concentration and higher strength as they can be distributed continuously in three dimensions smoothly without joints when compared to strut-based structures [21]. Furthermore, they have high surface area to volume ratio [22]. Thanks to these promising features, TPMS structures have been frequently studied in scaffold studies in the biomedical field [23]. In addition, the smooth and continuous surfaces they offer make them suitable for heat exchanger designs.

Each TPMS structure is controlled by mathematical equations defining $U=0$ condition as iso-surface boundary of solid and void parts [24]. There are numerous types of TPMS lattice topologies exist in the literature naturally since they are mathematical expression dependent structures. Some of them are Schoen's Gyroid, Schwarz Primitive, Schwarz Diamond, Fischer-Kosch S, Neovius' Surface, and so on. In this study, only three of these well-defined topologies are focused on: Schwarz Primitive, Schwarz Diamond, and Schoen's Gyroid.

2.3.1 Schwarz Primitive (Primitive) and Schwarz Diamond (Diamond)

The periodic minimum surface theory was first proposed by Hermann Schwarz and Edward Rudolf Neovius in 1880. The surface forms they put forward were basically composed of a continuous combination of the symmetries of the surfaces according to various axes in the unit cell [25]. Primitive and Diamond surfaces were named by Alan Schoen, who would define the Gyroid surface in the following century. Primitive is basically a union of primitive shapes constructed by Boolean operations. Due to its high surface-to-volume ratio and porosity, Primitive topologies can be used as tissue scaffolds [26]. On the other hand, Diamond is constructed by the interlocking of two harmonic labyrinths that can be exactly represented in terms of elliptic integrals [20].

2.3.2 Schoen's Gyroid

The gyroid shape was introduced by a NASA worker Alan Schoen in 1970. According to his research, the gyroid includes the Bravais lattice structure in BCC form. This lattice type is also related to Schwarz Diamond as an FCC structure, and the Schwarz Primitive family formed by primitive structures [27]. The implicit iso-surface equations for above-mentioned TPMS lattice types are given in the Table 2.1, and their unit cell illustrations are shown in the Figure 2.3.

Table 2.1 Implicit iso-surface equations ($U = 0$) for TPMS lattices [24].

TPMS	Iso-surface Equation
Primitive	$U_p = \cos(k_x x) + \cos(k_y y) + \cos(k_z z) - t$
Diamond	$U_D = \sin(k_x x) \sin(k_y y) \sin(k_z z) + \sin(k_x x) \cos(k_y y) \cos(k_z z)$ $+ \cos(k_x x) \sin(k_y y) \cos(k_z z)$ $+ \cos(k_x x) \cos(k_y y) \sin(k_z z) - t$
Gyroid	$U_G = \cos(k_x x) \sin(k_y y) + \cos(k_y y) \sin(k_z z) + \cos(k_z z) \sin(k_x x) - t$

Noting that $k_i = 2\pi \frac{n_i}{L_i}$, $i = x, y, z$ where n_i is cell repetitions, L_i is structure dimensions, and t is a variable that is used to modify volume fraction.

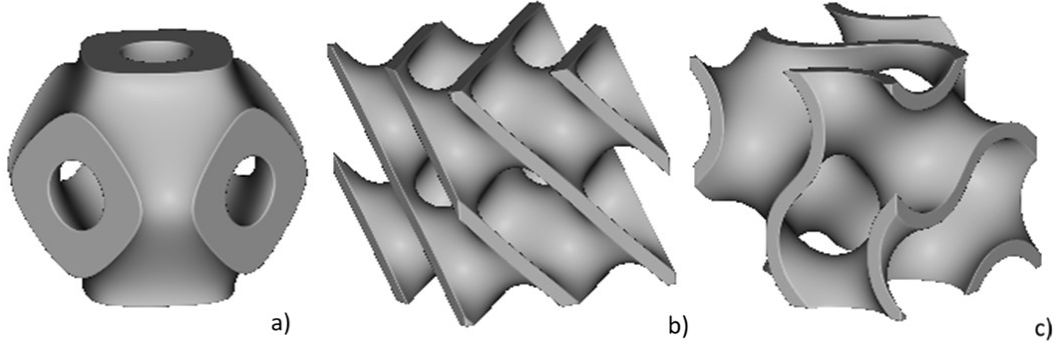


Figure 2.3. Unit cell representations of sheet TPMS lattices: a) Primitive b) Diamond c) Gyroid.

2.4 Mechanical Properties of Metallic Lattice Structures under Compression and Tension Loads

The behavior of all materials under load depends on their stiffness. Stiffness of lattice structures is generally assessed by Maxwell rule in the literature, which is discovered by Maxwell [28] and expanded by Calladine [29], and can be found by using Equation 1.

$$M = s - 3n + 6 \quad (1)$$

In this equation, “s” is the number of struts and “n” is the number of nodes. If Maxwell number is negative, bending stresses occur in the struts because there are not enough struts to balance the external loads. These structures show bending-dominated behavior which is preferable in the energy absorption and vibration isolation applications. If Maxwell number is positive, no bending occurs at the nodes, as the struts can balance external loads. These structures show stretch-dominated

behavior with superior stiffness to weight ratio [30]. FCC and BCC structures which to be investigated in this study are stated that showing bending-dominated behavior with Maxwell numbers of -14 and -13 respectively [31].

Lattice structures generally go through three stages under compressive loads: elastic, plastic and densification. In the elastic stage, the behavior of the lattice structure is elastic. When the yield limit is exceeded, the material deforms plastically. As can be seen in Figure 2.4, the stress required for plastically deform bending-dominated structures is constant whereas it decreases due to post-yield softening for stretch-dominated structures [15].

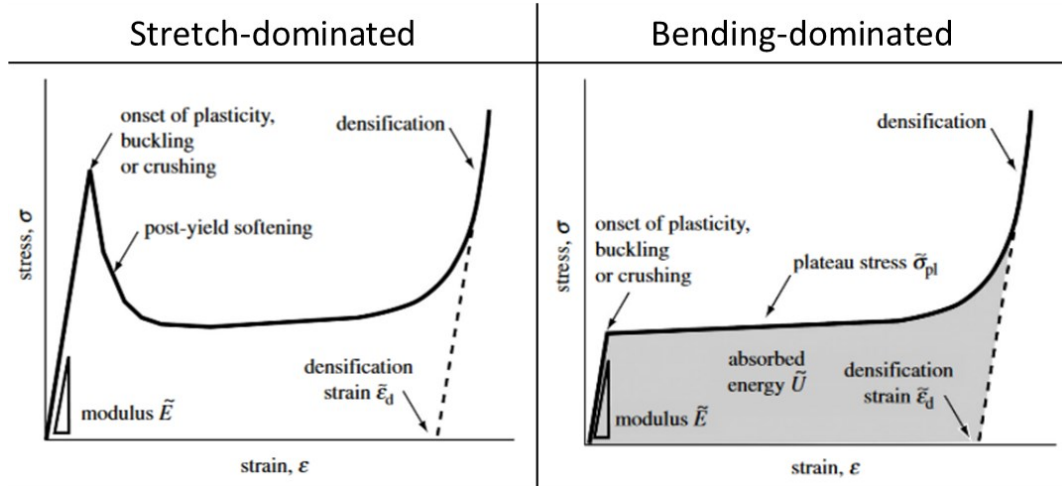


Figure 2.4. Stress-strain relation of stretch-dominated and bending-dominated lattice structures under compressive loads [15].

There are numerous studies in the literature focusing on the compressive behavior of metallic lattice structures. For example, Carlton et al. studied mechanical behavior of rhombic dodecahedron and octet-truss lattice structures with three different relative densities (10, 20 and 30 %) using SLM method. The authors stated that in the compression state, the octet-truss lattice structures show torsional behavior, whereas rhombic dodecahedron lattice structure is smoothly crushed [32]. Another study in the literature showed that cubic and diamond-shaped dodecahedron lattice

structures show stretch-dominated behavior while G7 lattice structures show bending-dominated behavior [33]. On the other hand, Maskery et al. studied the effect of unit cell size on the failure modes of double gyroid (DG) lattices. According to their results, the diagonal shear failure mode become dominant with the decrease in the cell size (see Figure 2.5) while localized low-strain fractures arises in larger unit cells. In addition, they revealed that the specific energy that can be damped by the heat-treated DG lattice is almost half of the compressive strain [34]. Kadkhodapour et al. showed that SLM manufactured Ti6Al4V lattice structures with stretch-dominated behavior such as cubic lattice structures go layer-by-layer deformation, while lattice structures with bending-dominated behavior such as diamond lattice structures are deformed along 45° lines under compressive loads [35]. Similarly, Vanderesse et al. stated that SLM manufactured Ti6Al4V cubic and diamond lattice structures were deformed layer-by-layer, and the BCC with additional strut in z direction was deformed along the 45° diagonal line [36]. In another study conducted with both skeletal and sheet TPMS structures in different volume fractions, it is seen that diamond and Neovious lattice structures have bending-dominated behavior while gyroid structures have stretch-dominated behavior [37].

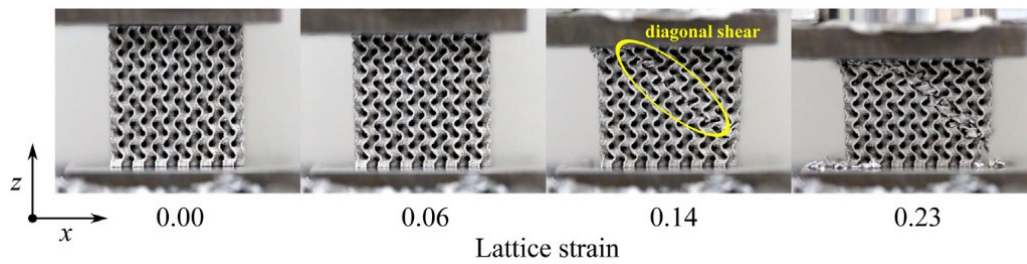


Figure 2.5. Diagonal shear failure mode in DG lattice with unit cell size of 3 mm [34].

Contrary to the studies examining the mechanical behavior of lattice structures under compression, the number of studies focusing on the behavior under tensile load is

very limited. This can be attributed to the lack of a standardized geometry for tensile testing, and the potential use of lattice structures in areas under compression load. In one of these studies, five strut-based and two skeletal-type TPMS topologies with same volume fraction and unit cell sizes are investigated under tensile loading. According to this work, PFCC topology which is FCC-based structure having additional struts in z direction showed highest load capacity along with the gyroid and BCC [38]. In another study conducted with Neovius and IWP TPMS lattices, it is shown samples with IWP had weaker stretch-dominated deformations according to their tensile responses (see Figure 2.6). In the same study, it is also revealed that the decreasing number of unit cells in a fixed design domain for both lattice topologies (meaning that increasing cell size) leads to decrease in the yield strength (YS) while increase in the elongation [39].

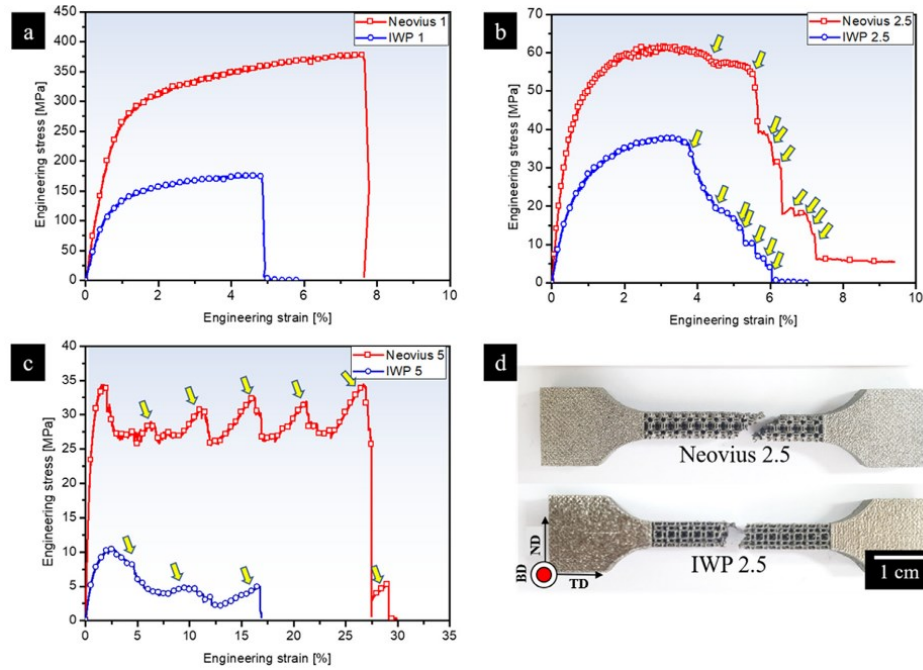


Figure 2.6. Tensile tests results of Neovius and IWP lattices with varying cell sizes [39].

Mechanical behaviors of different lattice structures are also compared in the literature. Rehme and Emmenmann stated that addition of struts in z direction to BCC or FCC increases their compressive strength [40]. Similarly, McKown et al. investigated the mechanical behavior of BCC and BCC with additional struts in z direction lattice structures produced by SLM. They stated that both lattices showed bending-dominated behavior and BCC with additional struts showed 2.5 - 3.5 times more YS than simple BCC lattices at different relative densities [41]. In another study, Xiao et al. investigated the mechanical behavior of FCC, vertex cubic and edge centered cubic lattice structures made up from 316L stainless steel by using SLM. They stated that the elastic modulus increased and the ability to absorb energy decreased with decrease in density. The authors also stated that FCC and vertex cubic lattice structures have higher mechanical properties than edge centered cubic structures [42]. Peng et al. compared mechanical behavior of simple cubic, simple cubic-BCC, BCC and FCC lattice structures and stated that simple cubic structure has the highest elastic modulus while BCC structure has the lowest elastic modulus. They also stated that the simple cubic structure was still in the elastic region even when other lattices exceeded the yield limit and were exposed to plastic deformation. Simple cubic-BCC and FCC structures behaved similarly in the elastic region, but simple cubic-BCC structure has higher stress in the plastic region [43]. Guo et al. studied mechanical properties of square, rectangular, tetrahedral and hexagonal lattice structures and stated that the hexagonal lattice structure gave the best result, and the tetrahedral lattice structure gave the worst result in terms of load bearing capacity [44]. On the other hand, Restrepo et al. investigated the mechanical performance of primitive, gyroid and diamond lattice structures, and stated that primitive structure has the highest elastic modulus and gyroid structure has the lowest compression strength [45].

In addition to the studies mentioned so far, there are also studies in the literature that specify the mechanical properties of lattice structures produced by EBM. For example, Khrapov et al. studied the effect of process parameters on tensile properties

of gyroid infill produced by Electron Beam Melting (EBM), and according to the results shown in Figure 2.7 represents that specimens produced with “Melt” theme have three times higher ultimate tensile strength than the “Wafer” theme samples. [46]. Furthermore, Hasib investigated the compressive mechanical properties of three different types of lattice structures (hexagonal, rhombic dodecahedron and octahedron) produced by EBM. He stated that the octagonal lattice structure had the highest and the hexagonal lattice structure has the lowest elastic modulus and compressive strength, and the octagonal lattice structure has the highest relative density [47]. In another study conducted by using EBM, it is investigated that the mechanical properties of cross, honeycomb and octagonal lattice structures. The authors stated that octagonal lattice structures showed the best performance in compression tests [48].

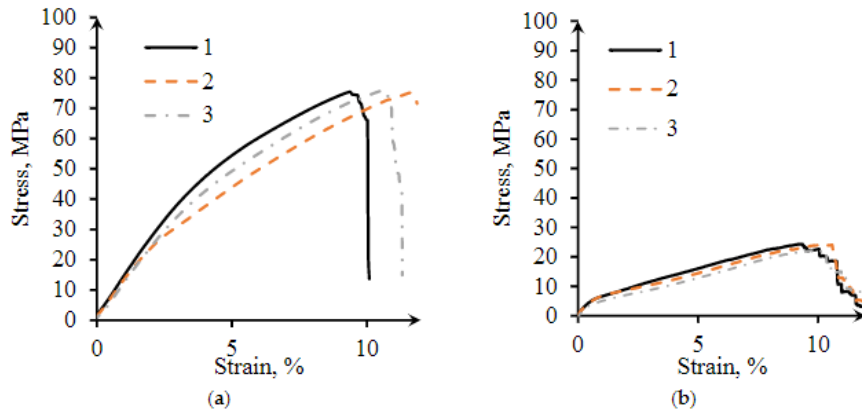


Figure 2.7. Tensile response of gyroid structures produced with different process parameters: a) Melt theme, b) Wafer theme [46].

There are few studies in the literature showing the mechanical responses of both strut-based lattices and sheet-based TPMS lattices with topologies to be used in this work. For example, the authors used primitive, diamond, gyroid, and BCC lattices in their study by using SLM with 316L stainless steel material. Based on the results (see Figure 2.8) they stated that TPMS lattice structures (especially diamond lattices) have higher strength, plateau stress and energy absorption capability than BCC

lattice structures [49]. Ahmadi et al. studied the mechanical properties of Ti6Al4V cubic, diamond, truncated cube, truncated octagonal cube, rhombic dodecahedron and rhombic octahedron lattice structures produced by SLM method. They divided the lattice structures as showing high rigidity (cube, truncated cube, truncated octagonal cube and rhombic octahedron) and low-hardness lattice structures (diamond and rhombic dodecahedron). It was stated that diamond lattice structure showed the lowest compressive strength, while the truncated cube showed the highest hardness [50]. Zhong et al. used SLM method to produce 316L stainless steel tetrakaidecahedron, diamond and BCC lattice structures. At the same density and unit cell size, the YS of the tetrakaidecahedron (9.67 MPa) was 59.83 % higher than the diamond structure (6.05 MPa) and 482.53 % higher than of the BCC structure (1.66 MPa). Similarly, the compression modulus of the tetrakaidecahedron (357.38 MPa) was 163.40 % higher than the diamond (135.68 MPa) and 1145.66 % higher than the BCC (28.69 MPa). This showed that the tetrakaidecahedron structure had much superior mechanical properties than diamond or BCC structure [51].

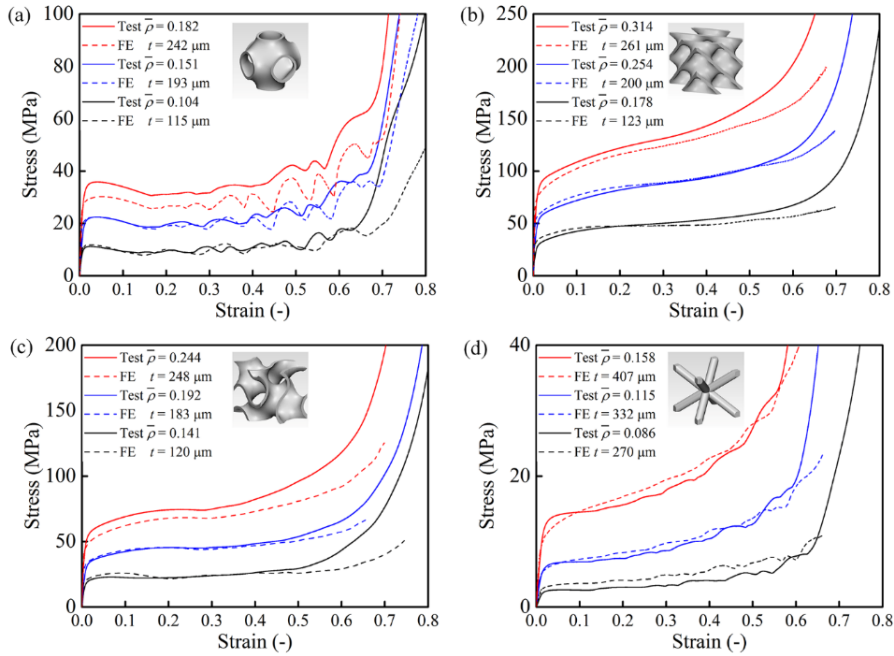


Figure 2.8. Comparison of strain-stress curves obtained from FEA and test results of four different lattices: a) primitive b) diamond c) gyroid d) BCC [49].

The literature review shows that there are very few studies that compare the mechanical properties of different lattice structures produced by EBM using same parameters, especially under both tensile and compressive loads. This thesis study aims to contribute to this gap in the literature.

CHAPTER 3

METHOD AND WORKFLOW

Design for additive manufacturing (DfAM) approach is a key point for the development of AM industry. Although the production-related design constraints seem to have disappeared and a much less restrictive production process has emerged, additive machines also have limitations that should be considered before production.

The limitations of the machines vary according to AM methods they are based on. This study mainly focuses on the constraints of the EBM technology since it is to be used in production. The design of lattice structures is highly interdependent process in this study, because the machine build size limits the use of conventional standard test sample sizes while the process parameters of manufacturing affect the unit cell design parameters, therefore the cell repetitions in testing cross sections.

In this section, after a brief explanation about the EBM system, the determination of the overall test sample sizes, the determination of the unit cell design parameters and the manufacturing constraints to be mentioned.

3.1 Electron Beam Melting (EBM)

The EBM method is a sub-branch of powder bed fusion systems, which is one of the seven additive manufacturing methods described in the Section 1. Powder bed fusion systems cover technologies that can produce parts from metal or polymer materials.

The EBM method along with the selective laser melting (SLM) method is a high-energy machine that allow the production of final parts using metallic powders. Arcam AB (Sweden) is the inventor, also the only manufacturer of the EBM method.

They patented their founding in 1993 as a method describing that layer-by-layer melting of an electrically conductive powder, by using electric beam to manufacture three-dimensional shapes. Today, they are still the sole supplier of this technology as a subsidiary of General Electric (US). The EBM takes place mostly in the aerospace industry and medical field. It has ability to tightly stack parts in the build chamber without having to support them from the baseplate which creates more productivity.

The melting of metal powders with EBM consists of successive steps and the repetition of these steps for each layer. The process starts with the heating of the build plate first, then the plate is lowered by one layer thickness and powder laying is carried out by recoater. Evenly distributed powders are loosely sintered by pre-heating. The next step is to melt the sections to be produced by a high-energy electron beam by contour or hatch scanning. After the melting is completed, the image of the whole table is taken with a high-resolution camera and this cycle continues until the production is completed by lowering the table one layer thickness.

The EBM system works under vacuum environment to make production more controlled since electrons are highly reactive toward environmental gases. The energy required to melt powdered metal is provided from high-power electron beam. Electron filament passes through a lens system (coils), then the beam is subjected to powder bed by scanning the current layer in XY plane with the help of deflection coils. The control of electron beam motion is provided by electronics rather than moving parts which makes it an inertia-free scanning system. Thus, the beam motion is fast and accurate. Furthermore, production in EBM is carried out at high temperatures. So, residual stresses are reduced to negligible levels and scattering of electrons is prevented by reducing the reactivity at elevated temperatures. This is achieved by a powerful 3 kW electron beam power and preheating system that can heat up the build chamber up to 1000°C before melting each layer.

Arcam EBM Q20plus device, provided by Turkish Aerospace for this study, is used which is especially developed for aerospace applications. Table 3.1 shows the

technical specifications of machine used in this study and Figure 3.1 illustrates the machine with a detailed layout of EBM system.



Figure 3.1. Arcam EBM Q20plus machine on the left and the layout of EBM system is on the right [52].

Table 3.1 Technical specifications of Arcam EBM Q20plus [52].

Maximum Build Size	350 x 380 mm (Ø x H)
Maximum Beam Power	3 kW
Cathode Type	Single crystalline
Minimum Beam Diameter	140 µm
Maximum EB Translation Speed	8000 m/s
Active Cooling	Water-cooled heat sink
Minimum Chamber Pressure	5 x 10 ⁻⁴ mbar
Typical Build Atmosphere	4 x 10 ⁻³ mbar (partial pressure of He)
He Consumption (Build Process)	4 l/h
He Consumption (Ventilation)	100-150 l/build
Power Supply	3 x 400 V, 32 A, 7 kW
CAD Interface	Standard: STL

Despite the unique features it offers, there are also issues and limitations where the EBM system is handicapped. These constraints, which have a direct impact on the part design, to be mentioned in the Section 3.2.3.

3.2 Modelling of Lattice Structures

Lattice structures are structures that can be expressed with mathematical equations, and therefore they can be obtained with different design methods. Among these methods, using software languages such as MATLAB and Python is common in literature studies, while the use of modules integrated into package design programs is more common in the industry.

There are several design programs in the market aiming to ease the design phase for additive manufacturing. Many existing CAD software providers such as Siemens NX (US), 3DEXperience from Dassault Systèmes (France), Netfabb from Autodesk (US) increase their design capabilities for additive manufacturing applications. In this study, nTopology (US) is selected to work throughout the design process since it fully focuses on additive manufacturing applications such as lightweighting by using lattices or topology optimization. Furthermore, nTopology uses an implicit modeling engine which represents bodies as mathematical equations, it enables complex designs to be easily modeled by performing design iterations rapidly, and it is easy to use since modeling operations are driven by “building blocks”.

The unit cell identification is the basic step of the lattice structure design, and it is characterized by the lattice type and material ratio to be utilized. In order to determine the material ratio in a unit cell, the relative density or volumetric ratio parameter is mostly preferred in the literature. For example, in their study Maskery et al. set the volume fraction property for lattices varying in overall size [53]. Additionally, Al-Ketan et al. followed a similar approach in their study as using pre-defined unit cell dimensions and volume fraction for varying lattice topologies [54]. In line with the approach applied in the literature, volume fraction is selected to

design all lattice structures to satisfy consistency of material ratio among all unit cells. Considering that both strut-based and TPMS topologies to be investigated in this work, usage of volume fraction also allows to satisfy consistency between two separate lattice families.

Strut-based topologies and TPMS topologies are controlled by different building blocks namely “Volume Lattice” and “Walled TPMS”. Both blocks require similar inputs which are a volume input that defines the design space to be filled with lattice, unit or fill type input for lattice type, unit size dimension inputs and a thickness input. Figure 3.2 shows these blocks with arbitrary unit cell parameters.

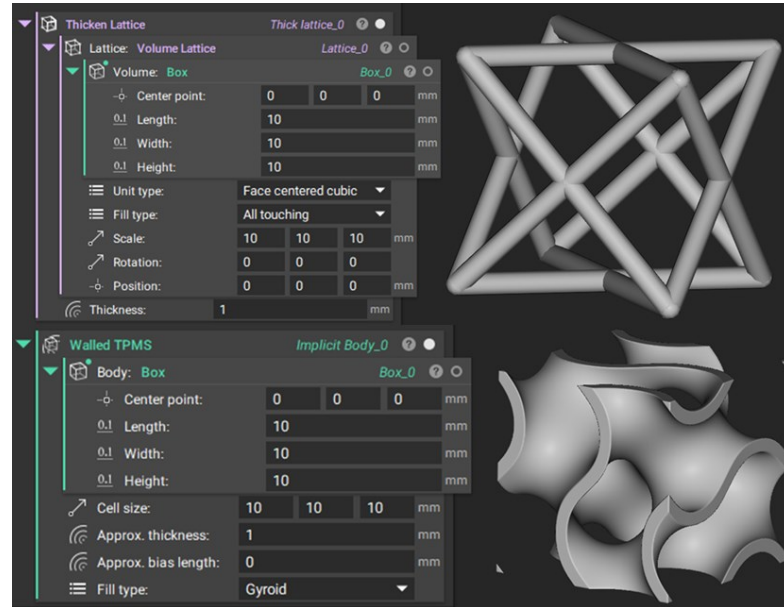


Figure 3.2. Volume Lattice building block and Walled TPMS building block.

As mentioned before, volume fraction to be used as a parameter in this study, but the unit cell creation blocks require a thickness input. To overcome this issue, "Relative Density" block is used for finding the thickness information required to create a unit cell. This block calculates the wall thickness or diameter by using a transfer function which is required to obtain the specified volume fraction (relative density) within defined unit cell dimensions for a given lattice type.

The rest of the design phase consists of creating the test geometries using blocks of Boolean operations. At the end, solid parts of specimens that designed independently of the lattice structure are combined with the lattice design space by using Boolean union operation. The dimensions and lattice parameters to be selected for the realization of this whole process depend on various limitations. In the remainder of this section, the determination of test geometries, the unit cell parameters and manufacturing constraints will be discussed.

3.2.1 Determination of Overall Test Geometries

Prior to selection of the unit cell size and volume fraction, the geometry of the test samples is required to be chosen because of the manufacturing limits of EBM. The tensile or compression test standard for additive manufacturing technologies has not yet been published by the standardization authorities, so different geometries are studied to see the behavior of materials. For example, long specimens with tapered grip sections are used in a recent study [46]. In another study, simple straight rectangular blocks are preferred with by using Gyroid in the middle [55]. Although different geometries are used for tensile testing in the literature, ASTM E8/E8M standard was taken into consideration as suggested in ASTM F3302 11.3 in this thesis [56].

The mechanical behavior of the lattice structure is affected by the patterns formed by the cells coming together, and as the number of cells increases the strength also increases [57]. The formation of such a cell number-controlled pattern is also possible with the rectangular sample type specified in ASTM E8/E8M FIG-1 (see Figure 3.3). The “Plate-Type” geometry proposed there is chosen to be adapted to the study, but the Overall Length size exceeds the build chamber height of the EBM machine. In the case where the build direction and the load application direction desired to be parallel, the compression samples are not considered at this stage since the dimensioning stage is driven by long samples to fit the batch height. Since the aim of the study is not to create a material database but to make a comparative

analysis of different topologies, it is considered to scale all the dimensions of the plate type sample by half to fit parts inside the build chamber. Determined part dimensions are shown in the Table 3.2.

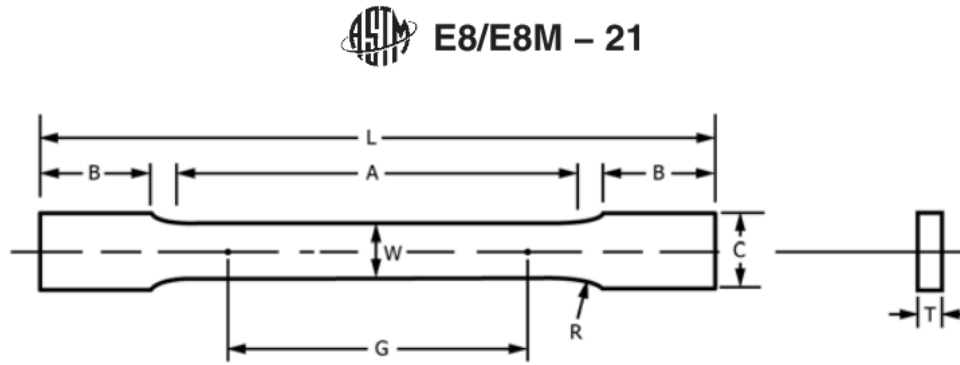


Figure 3.3. Tensile test specimen geometry to be used [58].

Table 3.2 Dimensions of tensile test specimen (all values are in mm)

	G	W	T	R	L	A	B	C
Original	200	40	-	25	450	225	75	50
Scaled	100	20	20	12.5	257	112.5	65	25

It should be noted that the grip section length (B) is longer than the scaled version of original size. It is modified according to the test setup requirement which dictates a minimum of 65~70 mm grip length to provide proper grip.

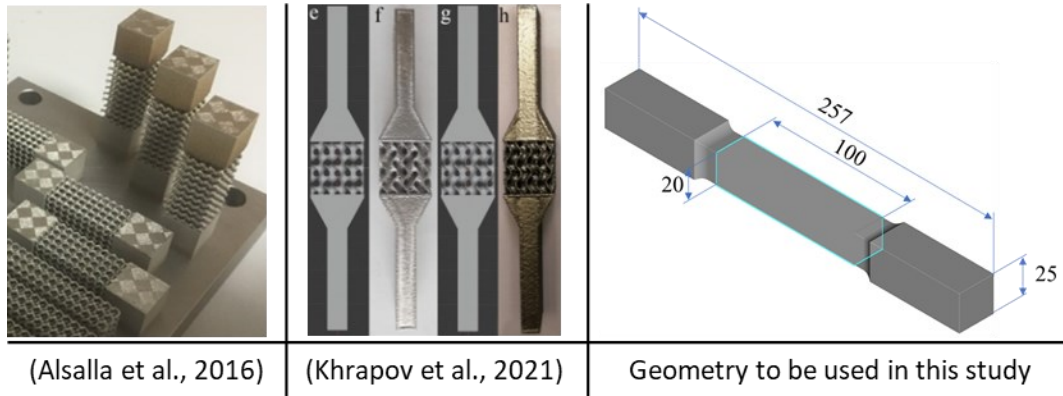


Figure 3.4. Comparison of the overall geometries for tensile testing.

After sizing the tensile test specimen, the geometry of the compression test specimens is determined. Contrary to the tensile sample for this study, there are guiding standards in the literature. ASTM F3302 S.10 recommends the ASTM E9 standard for compression tests [56], but ISO 13314 document published by ISO provides compression test standards for porous and cellular metals [59]. In this standard, it is recommended that the ratio of height to width should be between 1 and 2 for rectangular shaped specimens. Considering the necessity of using a minimum of three test specimens to obtain accurate test data, the size limit for the part placement on the production table, and the unit cell dimensions to be used, it was deemed appropriate to design the compression test specimens in dimensions of $40 \times 40 \times 40 \text{ mm}^3$. In addition, it is aimed to achieve a more balanced load distribution in the parts by adding 2 mm thick plates to the lower and upper surfaces of the samples in order to prevent premature failure in some cell elements in the load introduction region due to the low surface quality of the EBM products. Figure 3.5 shows the compression block design to be filled with lattice structures.

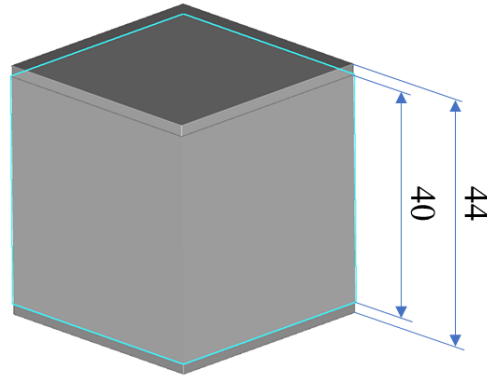


Figure 3.5. Overall geometry of compression test samples.

3.2.2 Unit Cell Parameters

After determination of overall dimensions of the tensile test sample, the unit cell size to be used in the gauge length section need to be specified. At this stage, the pore size takes importance, which is one of the factors that most affect the lattice structures to be produced with EBM.

The increase of the material ratio in the unit cells causes a decrease in the pore sizes, and smaller pore sizes lead to the powders to be trapped in the lattice due to sintering of non-used powders during the layer preheating specified in Section 3.1. On the other hand, arrangement of two cells or more in each direction on a cross-section is common approach. For example, in a recent study, tensile test geometries are designed for two different sheet TPMS lattices and the unit cells are dimensioned to fit 1, 2, and 5 rows of cells into the corresponding cross-sections of these geometries [39]. In another study, 5 mm and 7 mm wide bars were designed to perform the tensile test with the BCC topology. Unit cell sizing is studied under constant relative density with 1, 2, 3, 5 and 1, 2, 7 repetitions in related cross-sections respectively. As a result of the study, it is observed that the mechanical properties improved proportionally to the increasing number of unit cells [57]. Since it is commonly used in the literature, $5 \times 5 \times 5 \text{ mm}^3$ unit cell size is chosen which satisfies four cell repetitions in the testing cross section of tensile specimen geometry selected in the previous part.

The other critical parameter that defines a unit cell is the volume fraction. Besides it affects the amount of material that will fill a fixed volume, also requires consideration of another limitation that is the thin-wall manufacturability limit. In their study, Ameen et al. try to find the manufacturability limit of EBM system. They designed vertically oriented thin-wall plates and round bars with varying thickness or diameter values and finally determined that 0.6 mm is the minimum producible value for both plates and cylinders [60]. Furthermore, results obtained from industrial best practice reports [61] and previous productions with the machine used in this thesis suggest that 0.6 – 0.7 mm can be considered as the lower limit of manufacturability. Therefore, in the light of previous studies it is decided to set the lower wall thickness or diameter to 0.7 mm with a margin of safety to eliminate production disruption due to unpredictable errors. Among the topologies to be produced, it is observed that the lowest wall thickness in the same volume occurred in Primitive geometry, and the volume fraction that gives the wall thickness of 0.7 mm for the Primitive is found to be 50%. This value is applied to other topologies, and it is verified that none of topologies have less than 0.7 mm in wall thickness or strut diameter.

3.2.3 Manufacturing Constraints

Production parameters play a critical role in determining the mechanical properties of the final parts in all additive manufacturing methods. The EBM system offers the user different themes with fixed production parameters as standard which are namely “Melt”, “Net” and “Wafer” themes, and they have advantages over each other. In his doctoral study, Suard shows the difference between these standard themes clearly. According to his work, it is found that “Net” theme is successful for producing thin-walled structures up to 1 mm by applying low electron beam energy while the number and size of internal porosities increase in structures thicker than 1 mm. On the contrary, especially for structures thicker than 1 mm, “Melt” theme provides better dimensional accuracy compared to nominal CAD data and gives less porosity

inside the melted sections [62]. Figure 3.6 shows the compatibility comparison of “Net” and “Melt” themes with nominal CAD data on 1 mm struts having different build orientations while Figure 3.7 shows the large internal porosity observed in a 1.5 mm strut produced with “Net” theme.

The minimum thickness or diameter of all lattice structures (except Primitive) designed in this study is above 1 mm. Therefore, it is decided that would be more accurate to produce these parts using the “Melt” theme. Details of process parameters offered by the “Melt” theme are given in the Table 3.3.

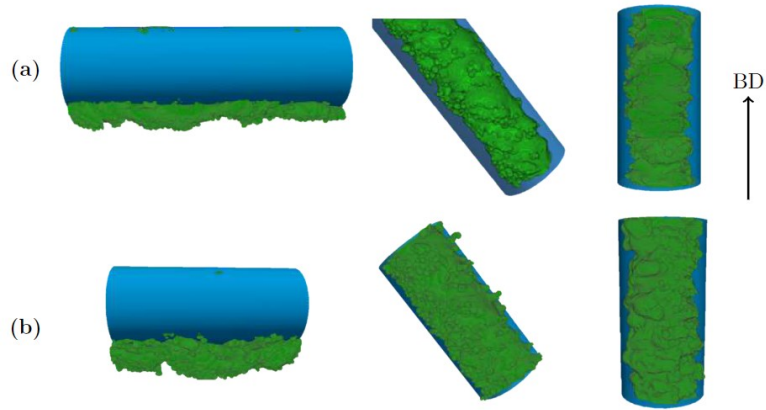


Figure 3.6. Comparison of struts in diameter of 1 mm produced with “Net” theme (a) and “Melt” theme (b) where blue regions represent nominal CAD data [62].



Figure 3.7. Section cut of a 1.5 mm strut produced with “Net” theme [62].

Table 3.3 Melt theme process parameters for Arcam EBM Q20plus.

PREHEATING	Focus Offset		44 mA	
	Heating Focus Offset		100 mA	
	Maximum Heat Time		60 s	
	Offset to Part		4 mm	
	Preheating 1		Preheating 2	
	Max. Beam Current	36 mA	Max. Beam Current	45 mA
	Beam Speed	40500 mm/s	Beam Speed	40500 mm/s
	Number of Repetitions	3	Number of Repetitions	3
MELTING	Surface Temperature		925 C	
	Number of Contours		3	
	Outer Contour		Inner Contours	
	Speed	450 mm/s	Speed	450 mm/s
	Current	9 mA	Current	9 mA
	Focus Offset	6 mA	Focus Offset	6 mA
	Offset	0.27	Offset	0.18
	HATCH			
	Beam		Hatch	
			Thickness	
	Manual Speed	4530 mm/s	Speed Factor	2.7
	Max. Current	28 mA		
	Focus Offset	45 mA		
	Speed Function	32		
			Line Offset	0.22
			Hatch Depth	0.09

Unlike laser powder bed fusion (L-PBF) systems, powder removal is a phenomenon that needs attention due to the application of high temperature and interlayer heating in EBM technology. Arcam provides a standard powder removal system named as Powder Recovery System (PRS) to both recover unused powder in the batch and removing semi-sintered powder left inside produced parts. PRS is offered as a standard, but there are additional powder removal methods have been tried in the literature due to unsuccessful powder removal even after this process. In their study, Khrapov et al. tried to remove powder from lattice scaffolds by using ultrasonic vibration (USV) method. It is observed that the applied method significantly reduces

the compressive mechanical properties of the parts, and they are stated that the use of PRS would be more beneficial until another new and effective powder removal method is developed [63]. In another study, researchers applied chemical etching process with different conditions after PRS to remove residual powder from lattice structures which are built in three different sizes and mesh densities. Although a decrease in the weight of the structures was observed between the lattices etched and unetched, there was no significant change in the amount of powder trapped in the cross sections and it was interpreted that this weight difference might depends on the decrease in diameter of the lattice struts [64].

Since an alternative powder removal method showing promising results has not been presented yet, it is anticipated that removing of residual powders to be done with PRS only, and studies focusing on this issue are researched. For example, in a study conducted with the application of PRS to samples containing different porosity sizes at different sample sizes, a relationship was established between the part thickness and the powder-removable porosity sizes [65]. If this linear correlation between the particle thickness and porosity size is extrapolated to the 20 mm part thickness in the tensile samples and 40 mm in the compression specimens to be used in this study as illustrated in Figure 3.8 , it is seen that the approximate porosity size of 2750 μm and 5300 μm is required for successful powder removal with PRS from tension and compression samples. Considering these results, it is decided to design alternative geometries with a new unit cell parameter set of 10x10x10 mm³ cell size and 25% volume fraction. Some of the approximate porosity sizes shown on the compression geometries in Figure 3.9 are measured as smaller than the value obtained by extrapolation. Increasing the porosities inside the unit cells designed with alternative parameter set further leads a single row of lattice in the gauge section of the tensile test specimens since the overall dimensions of test samples are already determined depending on the build chamber size. This situation will reduce the possibility of obtaining realistic data from the tests, so the alternative study continued with the selected unit cell parameters.

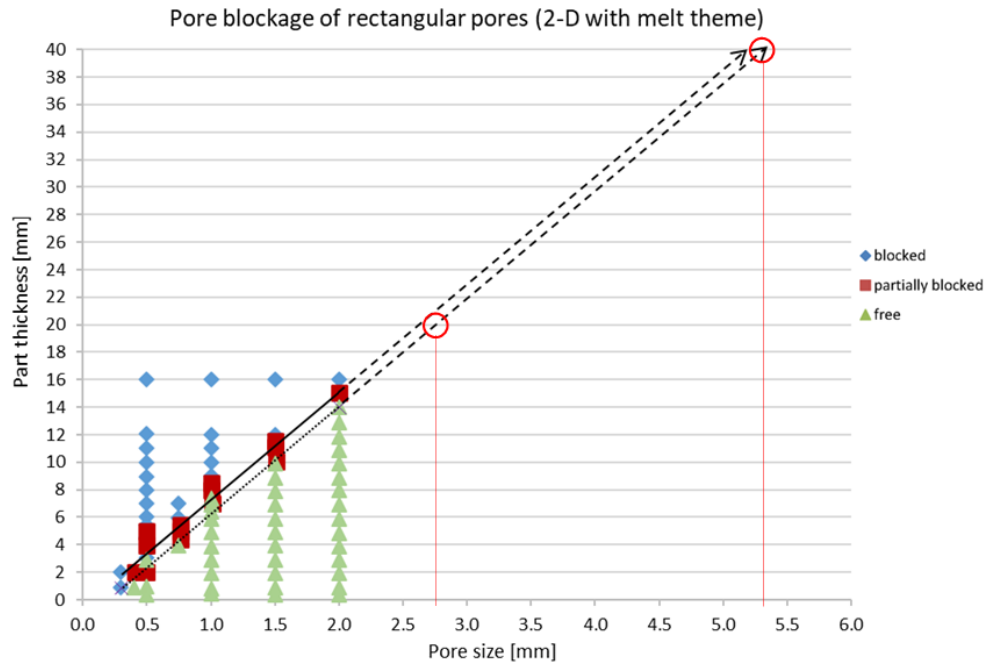


Figure 3.8. Extrapolated version of part thickness and pore size correlation for powder removal using PRS [65].

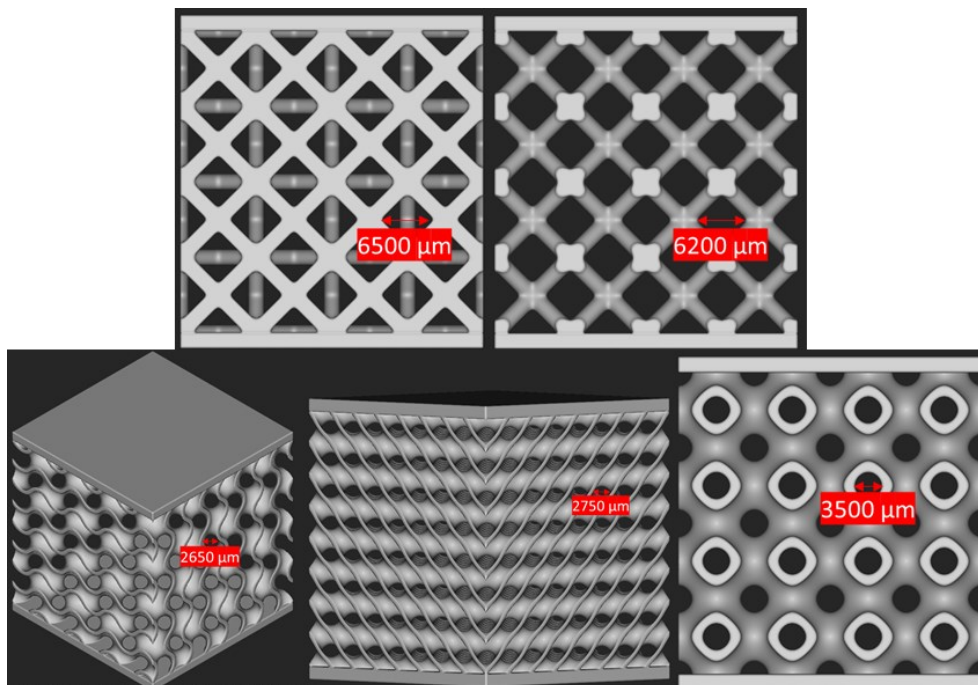


Figure 3.9. Pore sizes on CAD representations of alternatively designed lattices.

This new parameter set still ensures a minimum wall thickness of 0.7 mm in Primitive topology and provides at least two repetitions of unit cells along an edge of tensile specimen. With this alternative design, it is aimed to eliminate the time cost in case of unsuccessful powder removal in the lattice structures to be produced with the first parameter set. These parameter sets are denoted as “Configuration 1 (C1)” and “Configuration 2 (C2)” hereafter. The diameter and thickness values for the studied lattices are given in the Table 3.4.

Table 3.4 Strut diameter and wall thickness values for lattice types with two different parameter sets (all values are in mm).

	FCC	BCC	Primitive	Diamond	Gyroid
Configuration 1 (C1)	2.20	2.42	0.73	1.08	1.29
Configuration 2 (C2)	1.69	1.86	0.73	1.08	1.29

Prior to the manufacturing of specimens, there is another important point in the tensile test specimen that is the stress concentration occurring at the solid-lattice transition. Stress concentration caused by the sudden cross-section change in the solid-lattice transition region, which is not important for the compression test, can lead early fracture of the parts under tensile loading and cause unreliable test data. To overcome this phenomenon, it is thought that the lattices can be graded as they pass into the solid region, thereby increasing the cross-sectional area of the material in the region. In a study investigating this situation, it is shown that gradual increasing of strut diameters towards the load introduction area prevents early fracture of lattice section [66]. Therefore, a ramp function is used at two ends of the lattice region of the tensile test specimens to be able to double the thickness or diameter values at the last 15 mm towards solid section. Figure 3.10 shows the ramp function and illustration of FCC with and without gradual increase in the diameter.

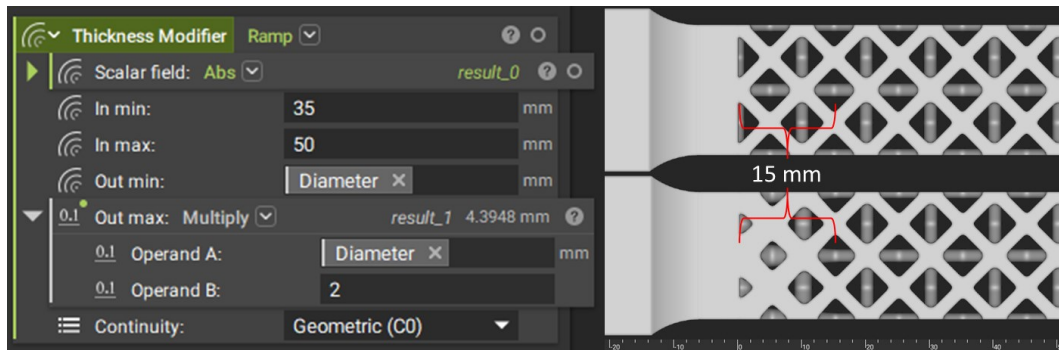


Figure 3.10. Ramp function used to grade diameter and thickness of lattices, and illustration of geometry with and without grading on FCC sample.

In addition to the absence of many studies in the literature on the increase in thickness and diameter in the solid-lattice transition zone, there is no accepted standard in the studies in which such trials are conducted. Therefore, the thickness increase is achieved by using ramp function in the region corresponding to one and half unit cell length towards solid section in this study. It is also aimed to provide input to the standardization studies for metallic AM tensile tests in the case of having successful results in all samples.

3.3 Manufacturing Stage

The last step before production is the build layout setup. Magics (Materialise, Belgium) software is used at this stage where manufacturing batch details such as production theme settings, support structures, part orientations, etc. are determined.

The orientation of the parts in the production circle is another production limitation, also a consideration. It is known that mechanical properties of additive manufacturing products highly dependent on build direction in general. For this reason, the build orientation is determined by considering the service loads for parts which functionality is sought. In a study on this subject, results obtained from tensile test specimens produced in different orientations with EBM show that yield and ultimate strengths do not change significantly depending on build orientation [67]. Besides, the orientation of parts is limited by the build chamber dimensions since all

test samples are desired to be produced in the same batch. Considering all these conditions, all parts are connected to the baseplate with supports and oriented vertically so that the loading direction in the tests and the production direction are the same. Ti-6Al-4V Grade 5 powders with 45-106 μm particle size provided from GE Additive (GE, United States) are utilized. The detailed composition of used powder is given in the Table 3.5.

Table 3.5 Chemical composition of Ti6Al4V powder provided by supplier.

	Al	V	C	Fe	O	N	H	Ti
Ti6Al4V Powder	6%	4%	0.03%	0.10%	0.15%	0.01%	0.00%	Balance

3.3.1 Production of Demo Parts

Considering the size and number of samples to be produced, a demo production with smaller parts is planned before the main production. In addition to the investigation of manufacturability of thin walls and powder removal capability, it is also aimed to eliminate the wasting both cost and time by producing the demo parts in case of inappropriate unit cell parameter selection while producing real test samples.

For demo production, pieces in 20x20x40 mm³ dimensions are designed for each lattice type, and flat surfaces with a thickness of 2 mm are added as a base surface to prevent them from being affected by the shearing forces during recoater motion. The isometric views of the designed demo parts are given in the Figure 3.11.

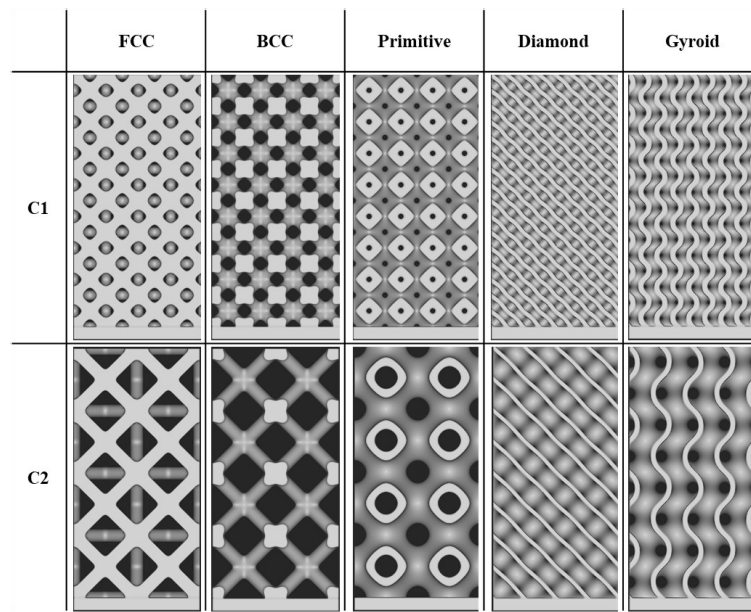


Figure 3.11. Demo production models for powder removal study.

The production of the demo parts is carried out using the “Melt” theme in accordance with the main test specimens. Figure 3.12 shows the produced parts after the standard PRS procedure is applied. The figure shows that powder removal process failed on the lattices produced with the C1 parameter set, and in addition, some of the existing pores have reached the level to be nearly closed. For parts with the C2 parameter set, successful removal of powders with PRS is achieved on BCC, FCC, and Primitive geometries, nevertheless the Gyroid and Diamond geometries are failed. Unlike the geometries produced with the first parameter set there is no porosity closures are observed in these geometries, so the trapped powder in the Gyroid and Diamond lattices can be removed manually with the help of a 1 mm diameter hand tool.

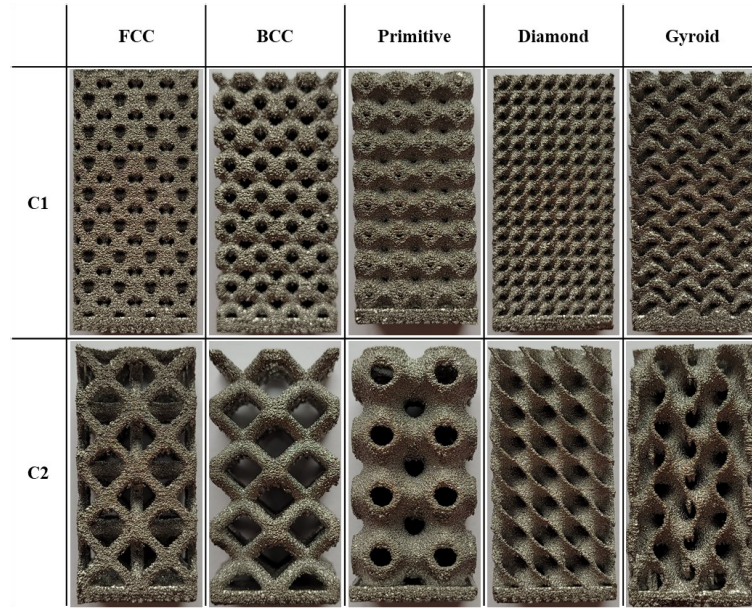


Figure 3.12. Produced demo parts after PRS and manual powder removal operation.

As a result of this production, the lattice parameters selected at the beginning of the study are evaluated as unsuccessful, and it is decided to continue working with the C2 parameter set which is considered as an alternative solution against the possibility of unsuccessful powder removal from lattices with initial design parameters.

3.3.2 Production of Test Samples

Based on demo production results, lattice sections of test models are updated with Configuration 2 parameters and transferred to the Magics software in the STL format to prepare the production batch.

Since the mechanical properties of materials produced by additive manufacturing are strictly dependent on the production method and process, it is decided to repeat the same test with at least three identical samples as recommended in ISO 13314 to obtain reliable test data. The dimensional limits of the EBM machine are taken into account while selecting the minimum recommended number of samples.

There have been many studies in the literature focusing on the placement of parts on the baseplate and its' effects on mechanical properties, microhardness, surface roughness, etc. For example, in a previous study on the machine used in this thesis report, the effect of part location on the mechanical properties is investigated. In the study carried out by placing the tensile test specimens at the corners and center of the rectangular base plate, it is observed that the mechanical properties are not significantly affected by the part placement, while the microhardness values are 4% higher in the parts placed on the edge due to the cooling effect [68]. Since the base plate to be used in this study is circular, although it has been shown in the previous study that effect of part location on affect mechanical properties is negligible, the tensile test samples are distributed radially around compression test samples which are arranged in 3 rows. Compression test specimens are attached to the support structures from their lower surfaces. Furthermore, depending on previous practices on the same machine, a gap of 0.32 mm is left between the upper surfaces and the support structure which prevents the cumulative transition of any possible deformation effect to the upper layers that exists at previous layers. Figure 3.13 and Figure 3.14 show the placement of the specimens on the base plate and the support connections of the compression test specimens, respectively.

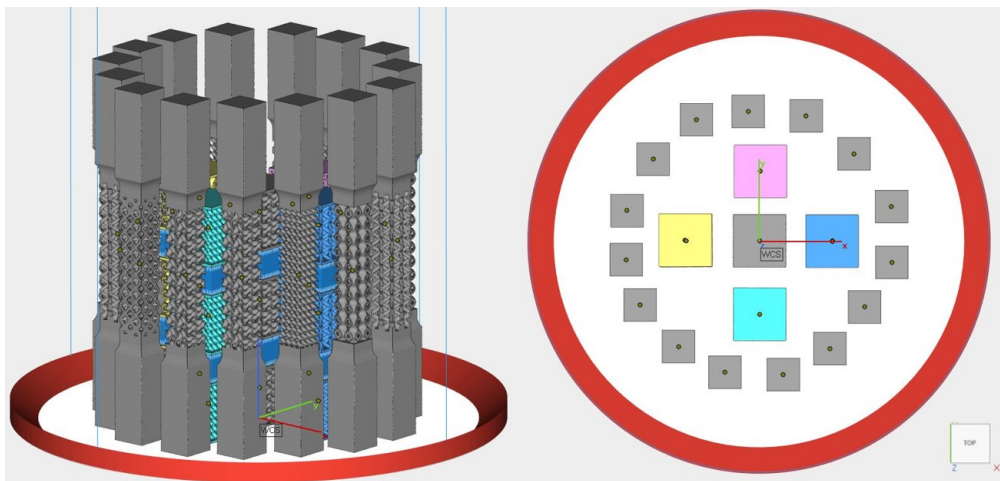


Figure 3.13. Distribution of parts on the build plate.

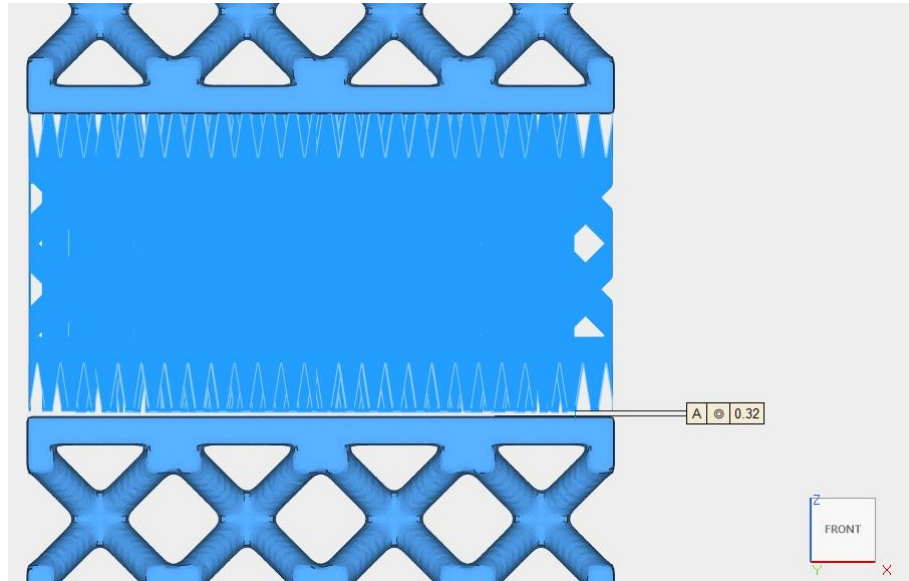


Figure 3.14. Gap between stacked compression test samples and support structures.

After the production completed, PRS is applied to remove the trapped powder from the parts. The semi-sintered powder stuck at the core of lattices is removed manually by using a thin hand tool since it is not possible to fully remove the trapped powder from these parts only with PRS. Figure 3.15 and Figure 3.16 shows the produced tensile and compression test specimens.

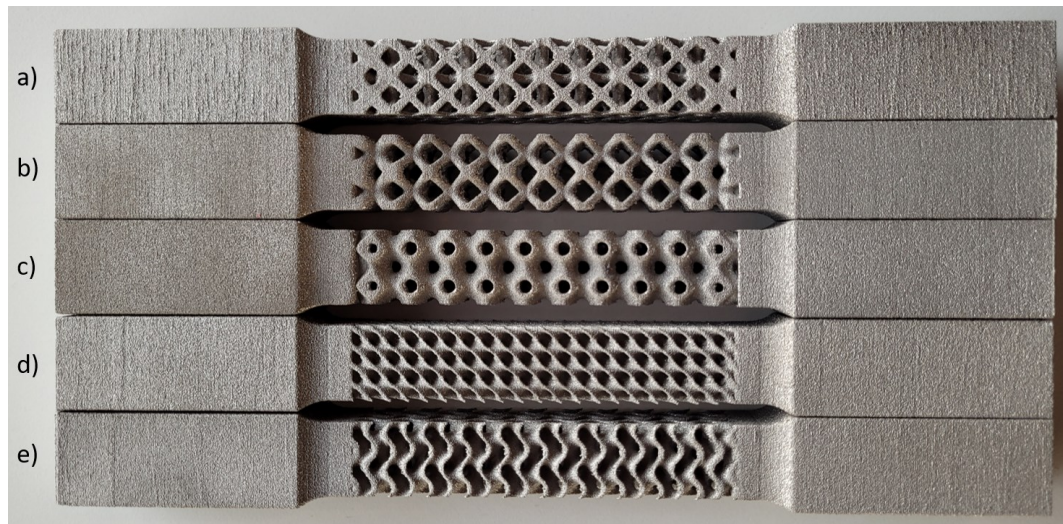


Figure 3.15. Tensile test specimens after powder removal: a) FCC b) BCC c) Primitive d) Diamond e) Gyroid

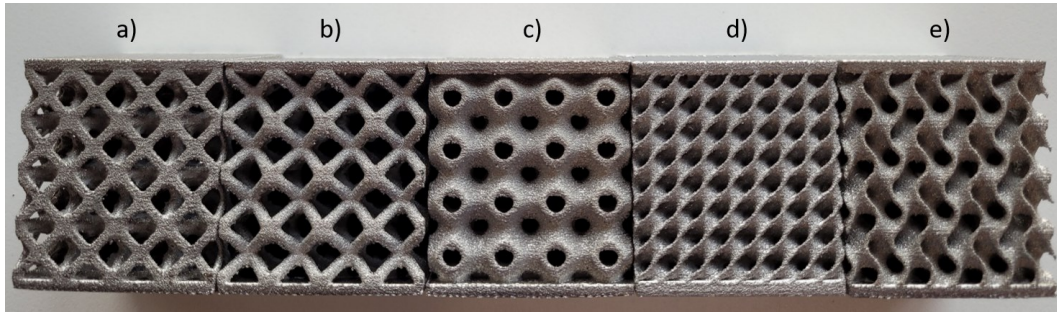


Figure 3.16. Compression test specimens after powder removal: a) FCC b) BCC c) Primitive d) Diamond e) Gyroid.

3.4 Experimental Study

Produced test samples are subjected to compression and tensile tests after powder removal and Scanning Electron Microscope (SEM) inspection. The ASTM E8/E8M standard procedure is followed for tensile testing and ISO 13314 is considered for compression testing. All experiments are done at room temperature under displacement-controlled condition with fixed strain rate of $1 \times 10^{-3} \text{ s}^{-1}$. ZwickRoell Z250 universal testing machine is used for tensile testing and Instron 5985 universal testing machine for compression testing. Both test setups have 250 kN load cells. Figure 3.17 shows tensile and compression testing machines.



Figure 3.17. Machines used in experimental study (Zwick Z250 and Instron 5985).

CHAPTER 4

RESULTS

4.1 Scanning Electron Microscope (SEM) Investigation

Compression samples were examined by SEM before testing. QUANTA 400F Field Emission SEM device was used for this process. By using SEM images, the diameters of the produced struts and the wall thickness of the sheet surfaces were examined as well as the satellite powder particles stuck to the melted parts.

The SEM images in Figure 4.1 show the excess of satellite powder particles that remain attached to the structure without melting on all surfaces. The preheating step of the EBM processes causes the temperature of the free particles to rise and become loose then stuck to the melted surfaces. It has been reported that for biomedical applications, these particles may cause inflammatory conditions if they are released in the body [69]. Furthermore, it has been shown that the particles on the surface can cause crack initiation formation by acting as a stress concentration zone on the part especially under fatigue applications [70].

The comparison of the thicknesses obtained from the SEM images with the nominal diameter or wall thicknesses is given in Table 4.1. The diameter and wall thickness measurements obtained from the images also revealed a high margin of error between the dimensions produced with the nominal geometries. Apart from the production-related parameters, it is thought that the thicknesses could not be measured by viewing them from the most accurate angle during SEM may also affected these errors.

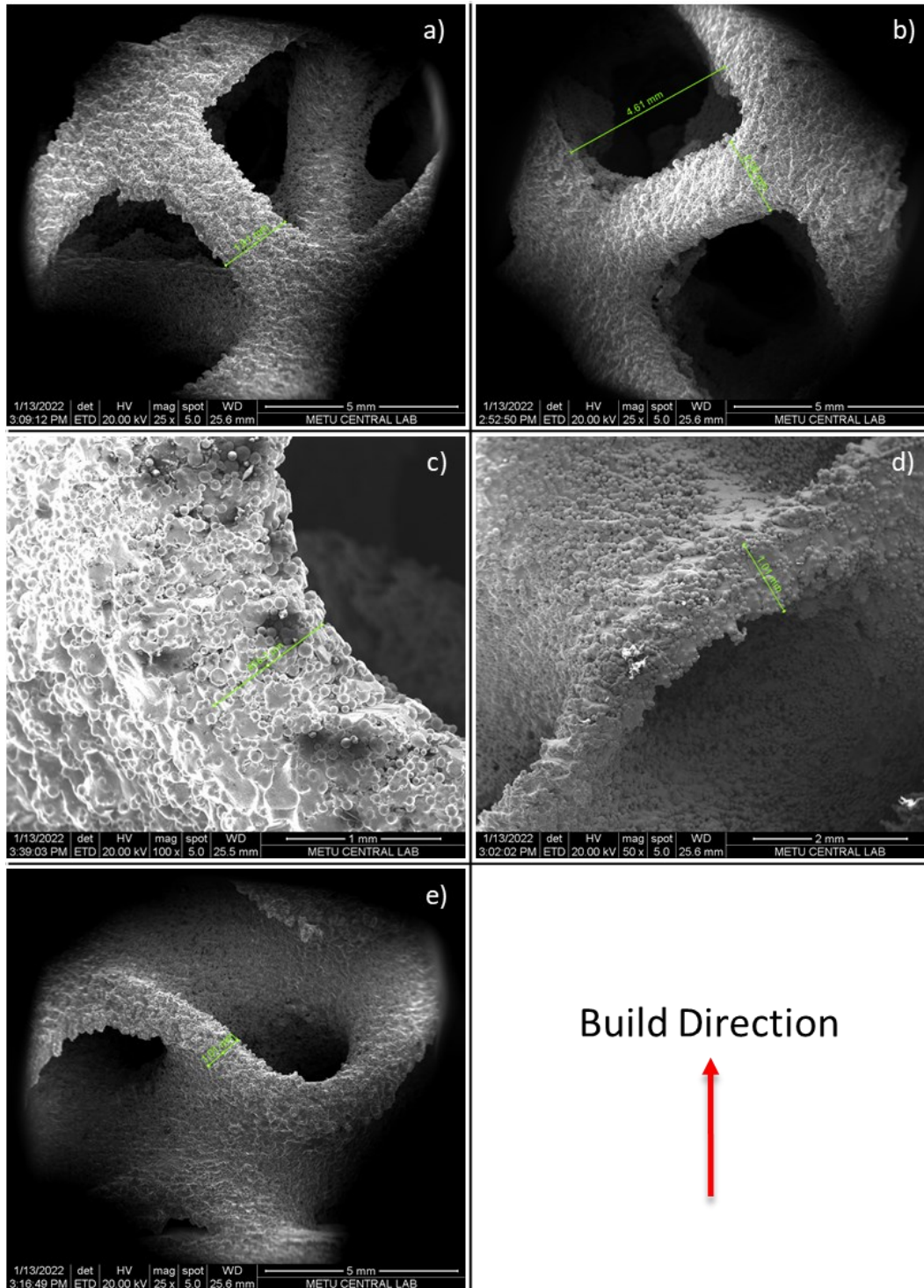


Figure 4.1. Thickness measurements on SEM images: a) FCC b) BCC c) Primitive d) Diamond e) Gyroid.

Table 4.1 Comparison of diameter and wall thicknesses.

	FCC	BCC	Primitive	Diamond	Gyroid
Nominal (mm)	1.69	1.86	0.73	1.08	1.29
Produced (mm)	1.91	2.06	0.86	1.01	1.01
Error (%)	-13.0	-10.7	-17.8	6.5	21.7

In Figure 4.2.a and Figure 4.2.c, existing porosities on struts are marked with circles. As previously addressed by Chan et al., these porosities act as stress concentration and crack initiation regions depending on their depth. On the other hand, it has been stated in the literature that the amount of unmelted particles adhering to the lower and upper surfaces is different depending on the build direction [39]. This situation is also observed and elliptically marked both in Figure 4.2.a and Figure 4.2.b. It can be seen from these figures that the amount of powders stuck to the upper surface regions is relatively less than other regions. It has been stated in the same study that this situation does not have a significant effect on the mechanical properties. In addition, the presence of the staircase phenomenon seen in most of the additive manufacturing methods is also observed in Figure 4.2.c.

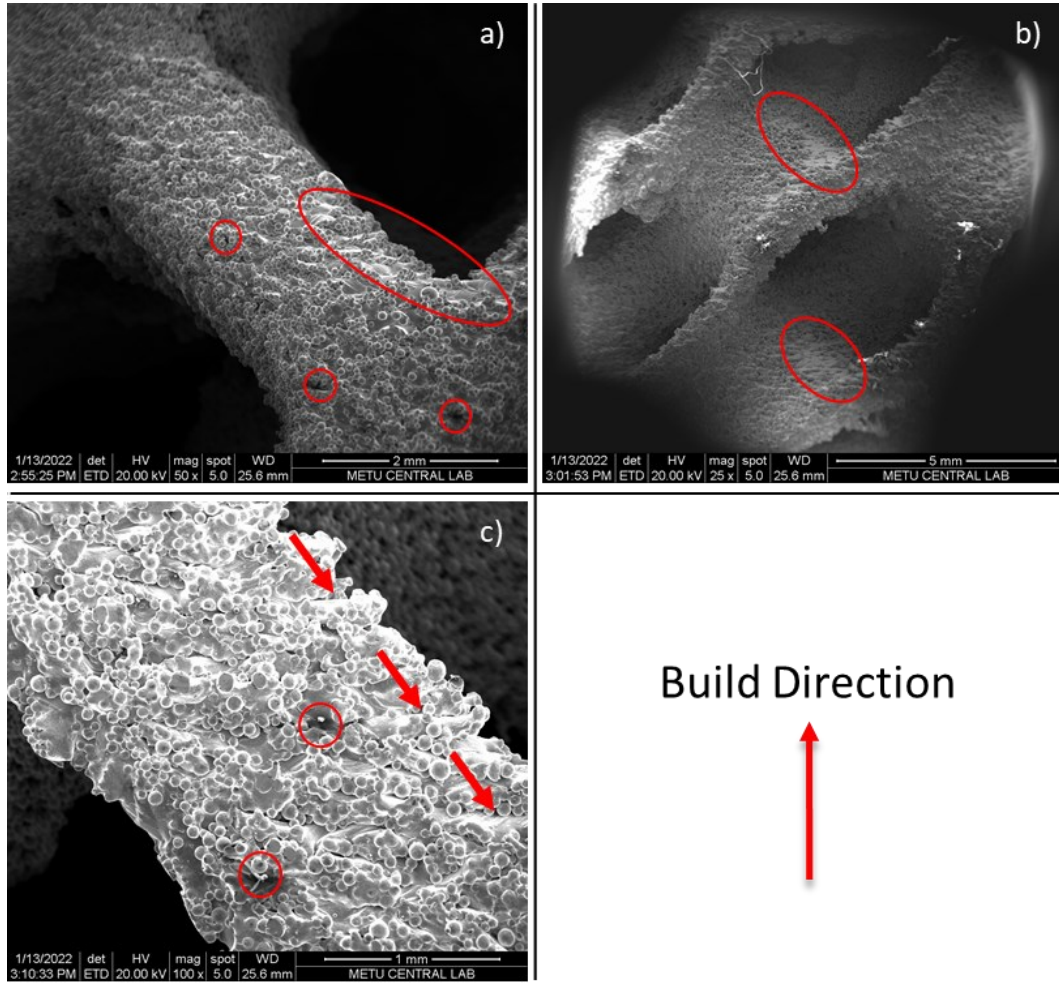


Figure 4.2. Detailed SEM images of production related defects.

4.2 Comparison of Test Results

4.2.1 Tensile Test

As a result of the tensile tests, the load and displacement relationship are obtained for all 15 samples. These data then are converted into nominal stress – nominal strain graph by using Equation 2 and Equation 3 to compare with the FEA results, and to obtain the lattice topology dependent mechanical properties.

$$\sigma_0 = \frac{P}{A_0} \quad (2)$$

$$\epsilon_0 = \frac{l - l_0}{l_0} \quad (3)$$

There are different approaches in the literature for cross-sectional area in the calculation of nominal stress. In one study, researchers took the cross-section of lattice part as 1600 mm² assuming that the part is solid in dimensions of 40x40x40 mm [24]. On the other hand, the average of the maximum and minimum cross-sectional areas was used in another study to consider the effect of the varying cross-sections through the lattice[71]. In this study, the average cross-sectional area approach is used for the nominal stress calculation, and the calculated minimum, maximum and average cross-sectional areas for each topology are shown in Table 4.2.

Table 4.2 Sample cross-sections for each topology used in tensile tests.

Section Area	FCC	BCC	Primitive	Diamond	Gyroid
Maximum (mm²)	207.86	117.88	138.84	137.02	123.03
Minimum (mm²)	49.06	51.79	77.74	78.95	83.81
Average (mm²)	128.46	84.83	108.29	107.99	103.42

The comparative graph of the mechanical behavior of lattice topologies under tensile load is given in Figure 4.3.

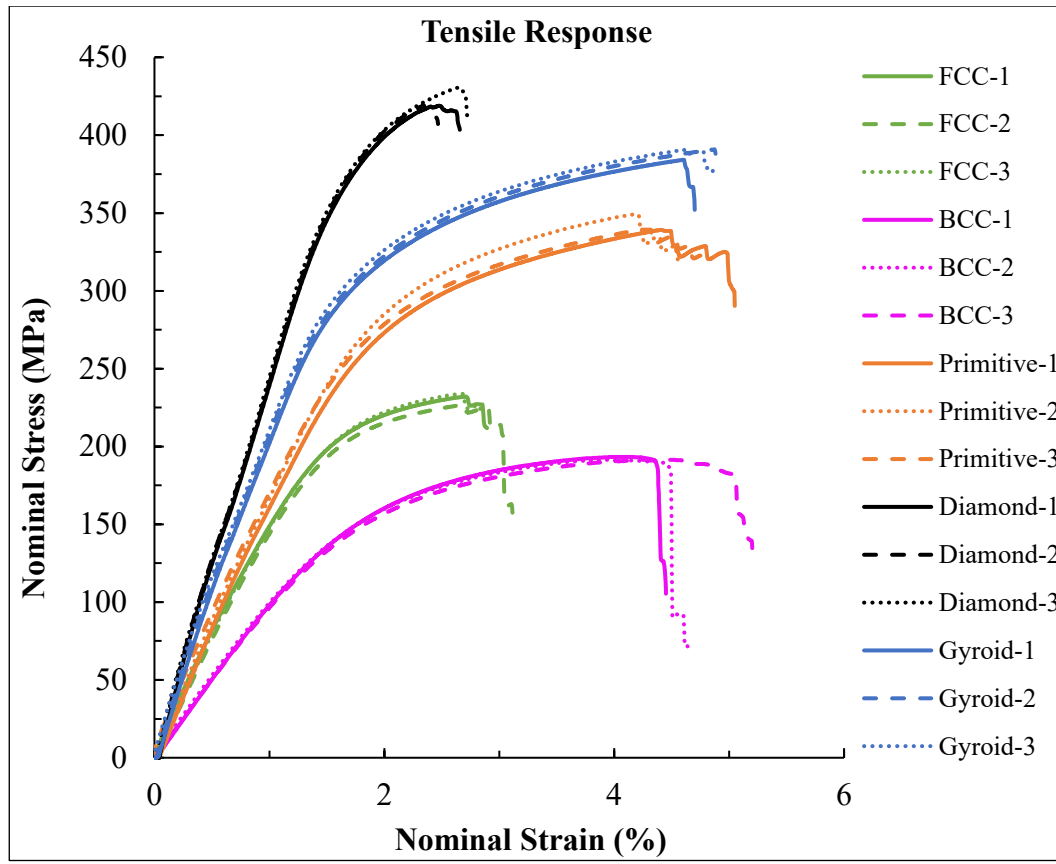


Figure 4.3. Tensile behavior comparison of different lattice topologies.

If the graph is examined, it is seen that reproducible and highly correlated results are obtained for each lattice topologies. The failure of the lattices occurred cell by cell during the experiments, and this can also be seen from the sudden drops immediately after reaching the ultimate tensile strengths in the result graph. Among all samples, Diamond showed the highest ultimate tensile strength (UTS) (422 MPa) with the lowest elongation value (~2.5%) and fractured in a brittle form while BCC showed a ductile behavior by showing the lowest UTS (192 MPa) at high elongation (~4.5%). On the other hand, Diamond had the highest strength and Primitive had the lowest strength while Gyroid and Primitive showed similar strain at the fracture which confirms the comparative results of Zhang et al.'s work with Diamond, Gyroid, Primitive and BCC [49]. In addition, tensile test results showed that TPMS topologies have approximately two times higher strength than strut-based topologies (see Table 4.3). This can be attributed to main properties of TPMS lattices which are

reducing stress concentrations by eliminating joints and having more stable failure mechanisms. The elastic modulus, yield strength and UTS values obtained from the tensile test results are given in Table 4.3.

Table 4.3 Mechanical properties of lattices obtained from tensile tests.

	Elastic Modulus, E (GPa)	Yield Strength, σ_y (MPa)	Ultimate Tensile Strength, σ_u (MPa)
FCC	16.17 ± 0.23	183 ± 4	228 ± 12
BCC	9.69 ± 0.15	145 ± 4	192 ± 4
Primitive	16.29 ± 0.36	269 ± 7	334 ± 13
Diamond	24.03 ± 0.12	383 ± 4	424 ± 10
Gyroid	20.25 ± 0.38	302 ± 3	388 ± 2

Remark: Values are in form of means \pm SD (n = 3).

4.2.2 Compression Test

The compression tests applied to the remaining 15 samples and were carried out in accordance with the ISO13314:2011 standard. Compressive properties of each lattice topology are then derived by using the load-displacement data obtained from experiments.

Like the approach used to calculate stress-strain diagrams from tensile test results, the same diagrams for compression parts are also derived using the mean of the maximum and minimum cross-sectional areas given in the Table 4.4. Corresponding comparative stress-strain curves of all lattices are provided in the Figure 4.4.

Among the compressive properties, the quasi-elastic gradient is the gradient of the straight line lying on the linear deformation region at the beginning of the curve and the compressive offset stress (often referred as compressive yield strength) is the stress level at the plastic compressive strain of 0.2% (see Figure 4.5). First maximum compressive strength is found as the first local maximum in the curve and the plateau stress is calculated as the arithmetical mean of the stresses in the compressive strain

interval between 20% and 40%. Finally, the energy absorption capability is found as the area under compressive stress-strain curve up to 50% strain level for each lattice.

Table 4.4 Sample cross-sections for each topology used in compression tests.

Section Area	FCC	BCC	Primitive	Diamond	Gyroid
Maximum (mm²)	829.94	472.27	554.77	546.98	491.66
Minimum (mm²)	192.88	212.54	310.96	315.57	335.21
Average (mm²)	511.41	342.41	432.86	431.28	413.44

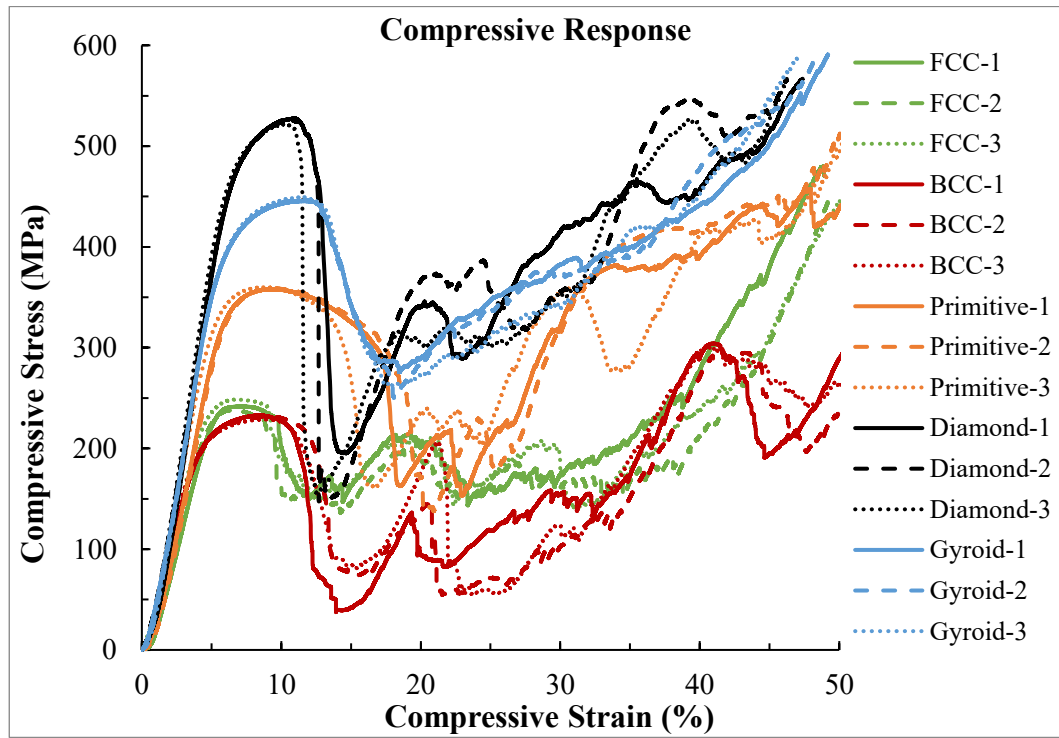


Figure 4.4. Compressive behavior comparison of different lattice topologies.

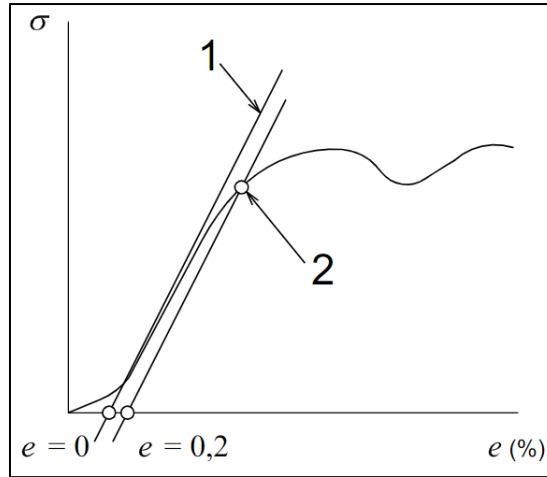


Figure 4.5. Stress-strain curve showing the quasi-elastic gradient and compressive offset stress.

Table 4.5 Mechanical properties of lattices obtained from compression tests.

	Quasi-elastic Gradient, E_{qe} (GPa)	Compressive Offset Stress, σ_y (MPa)	First max. Compressive Strength, σ_e (MPa)	Plateau Stress, $\sigma_{pl\ 20-40}$ (MPa)	Energy Absorption, W_{50} (MJ/m ³)
FCC	5.73 ± 0.18	207 ± 6	242 ± 6	183 ± 11	103.4 ± 5.9
BCC	5.78 ± 0.15	175 ± 4	231 ± 2	142 ± 16	84.2 ± 3.3
Primitive	7.09 ± 0.22	307 ± 13	360 ± 1	300 ± 2	157.8 ± 1.6
Diamond	8.97 ± 0.3	427 ± 17	526 ± 5	394 ± 11	176.6 ± 5.8
Gyroid	8.37 ± 0.13	304 ± 1	448 ± 2	367 ± 10	180.2 ± 7.1

Remark: Values are in form of means \pm SD (n = 3).

Compressive properties of lattices calculated as explained above are provided in the Table 4.5. It can be drawn from experimental results that Diamond had the highest yield stress with 427 MPa and first maximum compressive strength with 526 MPa while BCC and FCC were yielded at lower stress levels (207 MPa and 175 MPa, respectively). Although the compressive offset stresses of Primitive and Gyroid are almost similar, Gyroid outperformed over the Primitive on the first maximum compressive strength with 448 MPa. These results are consistent with the tensile test

work of this thesis and the study done by Zhang et al which is previously referred in the Section 2.4 [49]. Additionally, Gyroid showed compromising results on the plateau region by having 367 MPa mean stresses following the Diamond (394 MPa). Interestingly, Gyroid had the best energy absorption capability among all lattices with 180.2 MJ/m^3 while BCC gave lowest results as 84.2 MJ/m^3 meaningly Gyroid has resistance against compressive deformations more than twice the BCC. The obtained results support the study conducted by Maskery et al. where they observed the heat-treated double gyroid topology can absorb three times more energy compared to BCC [34]. This performance can be attributed to the smoother transitions between unit cell surfaces of Gyroid topology. Additionally, results obtained from compression tests support the findings in the study of Al-Ketan et al where they determined sheet-TPMS topologies show stretching-dominated behavior [54].

In addition to the mechanical properties, the failure mechanisms of each topology are also examined with the help of video recording throughout the compression tests. Captured images at each 10% strain increment for all topologies are provided in Figure 4.6. At 10% strain, all topologies showed similar behavior as going under barrel-like deformation. Further increase in the strain leads diagonal shear band failure at all specimens except FCC. FCC specimens are fractured at first and last rows, and at the end of the test there is still one cell layer kept its integrity. Findings on the failure mechanisms of TPMS lattices partially confirm the test results of Sun et al. in which they used the same sheet-based TPMS topologies, but with different manufacturing method (SLM) and volume fractions [72]. As seen in Figure 4.6, while all TPMS lattices in this study showed a diagonal shear band, they detected progressive layer-by-layer failure in the Primitive structure starting from the mid-layer. This difference can be a strong evidence of mechanical response dependency in lattice parts to both production method and unit cell design.

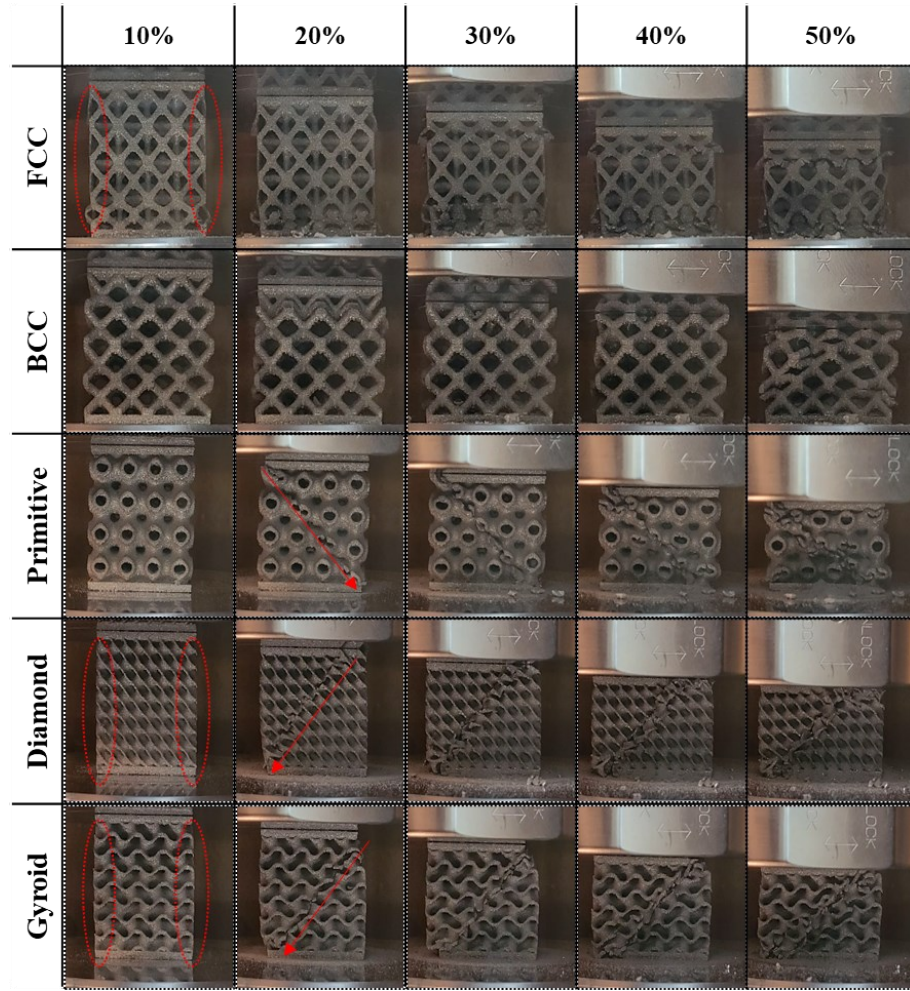


Figure 4.6. Compression test stages with 10% strain increments.

4.2.3 Theoretical Model

The commonly accepted method in the literature for selecting the lattice volume fraction or relative density proper for mechanical applications of lattice structures under compressive loading is to use the semi-empirical equations derived from experimental results by Ashby [15]. The formulas derived for the structures showing bending-dominated and stretch-dominated behavior are given in the Table 4.6.

Table 4.6 Mechanical property formulations of lattices based on relative densities and response types.

Bending-Dominated		Stretch-Dominated	
$\frac{E_{latt.}}{E_{sol.}} = C_1 \left(\frac{\rho_{latt.}}{\rho_{sol.}} \right)^2$	(4)	$\frac{E_{latt.}}{E_{sol.}} = C_1 \left(\frac{\rho_{latt.}}{\rho_{sol.}} \right)$	(6)
$\frac{\sigma_{pl.latt.}}{\sigma_{y.sol.}} = C_5 \left(\frac{\rho_{latt.}}{\rho_{sol.}} \right)^{3/2}$	(5)	$\frac{\sigma_{pl.latt.}}{\sigma_{y.sol.}} = C_5 \left(\frac{\rho_{latt.}}{\rho_{sol.}} \right)$	(7)

In equations from (4) to (7) E and ρ indicate modulus and density where their subscripts “latt.” denotes property of solid material and “sol.” is for related bulk material. Ratio of densities are also treated as volume fraction. On the other hand, $\sigma_{pl.latt.}$ shows the plateau stress of the lattice while $\sigma_{y.sol.}$ is indicating the yield strength of the bulk material.

To assess the experimental results with the theoretical model, produced volume fractions of the parts are measured using Archimedes’ method. METTLER TOLEDO (USA) XS204 device with maximum capacity of 220 g and readability of 0.1 mg is used for density measurements (see Figure 4.7). Due to the mass limitation of the machine, previously produced demo samples are utilized. To eliminate the bubbling of liquid at the lattice cell surface, laboratory grade ethanol is used which has lower surface tension (22.27×10^{-3} N/m at 20 °C) than pure water [73].



Figure 4.7. METTLER TOLEDO XS204 analytical balance device.

Based on the previously studied metal foam data, Ashby et al. provided a range of values that are 0.1-4.0 and 0.1-1.0 for coefficients C_1 and C_5 , respectively. As BCC and FCC are lattices with negative Maxwell number as shown in Section 2.4, they are considered as bending-dominated structures and Equation (4) and (5) are used to calculate related Gibson-Ashby coefficients. On the other hand, Al-Ketan et al. concluded that the sheet-based TPMS lattices exhibit stretch-dominated behavior, which is consistent with the results shown in Section 4.2.2 [54]. Depending on these findings, TPMS lattices investigated in this study are subjected to the Equation (6) and (7). Measurement results along with analytical solution based on experimental data are provided in Table 4.7. It can be drawn from results that the C_1 coefficient is in the appropriate range for all lattices. However, the C_5 coefficient is at the limit of 1.00 for Primitive and Gyroid, while it was above this value for other topologies. Maconachie et al. stated that the inconsistency between the experimental and theoretical results may be arisen from the overestimation in the density measurements by using Archimedes' method [74]. Considering the relative density results in Table 4.7, limit-exceeding results for C_5 in this study can also be attributed to their approach.

Table 4.7 Gibson-Ashby coefficients derived from experimental results.

	Relative Density (ρ^*)		E^* ($\times 10^{-3}$)	C_1	σ^* ($\times 10^{-3}$)	C_5
	Nominal	Measured				
FCC	0.25	0.282	36.3	0.4563	194.7	1.3006
BCC		0.256	36.6	0.5589	151.1	1.1674
Primitive		0.326	44.9	0.1376	319.1	0.9790
Diamond		0.340	56.8	0.1669	419.1	1.2323
Gyroid		0.385	53.0	0.1377	390.4	1.0145

4.3 Comparison of FEA and Test Results

Both compressive and tensile responses of experimentally tested lattices are also studied by conducting nonlinear static FEA. To prepare analysis model, HyperMesh (Altair, US) software is used and analyses are driven on OptiStruct (Altair, US), an implicit solver. Since a similar approach is applied previously in the literature [24], material properties required for finite element modelling is taken from performed tensile and compression test results provided in Table 4.3 and Table 4.5. Poisson's ratio is taken 0.34 as an average value for Ti6Al4V alloys.

The design information of produced samples are already extracted from nTopology in STL format. So, these models are imported to HyperMesh then the triangular shell elements (tria3) are converted to four-node solid tetrahedral elements (tetra4). Rigid body elements (RBE2) are assigned to both upper and lower surface nodes of either specimen types. All degrees of freedom (DOF) of independent node belonging to lower surface RBE2 are fixed while the third DOF (dof3) for independent node of upper surface RBE2 which represents the displacement of load cell head is set as displacement value at failure from corresponding tests. Figure 4.8 and Figure 4.9 illustrates the boundary conditions on both tensile and compression test specimens.

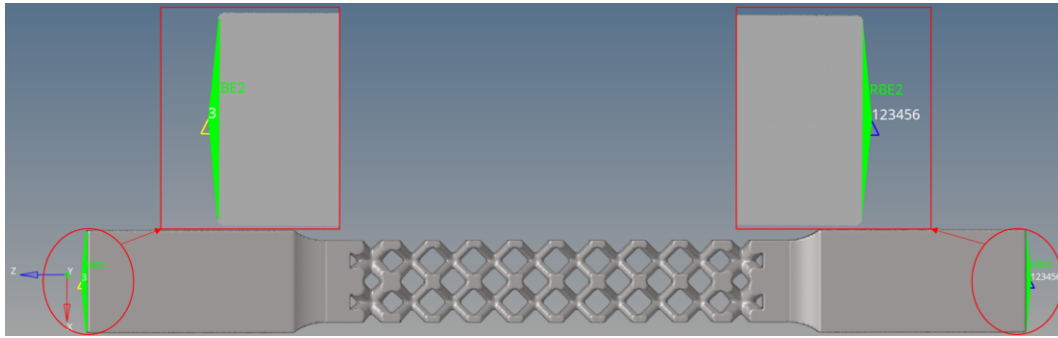


Figure 4.8. FEA boundary conditions of tensile test specimen with BCC.

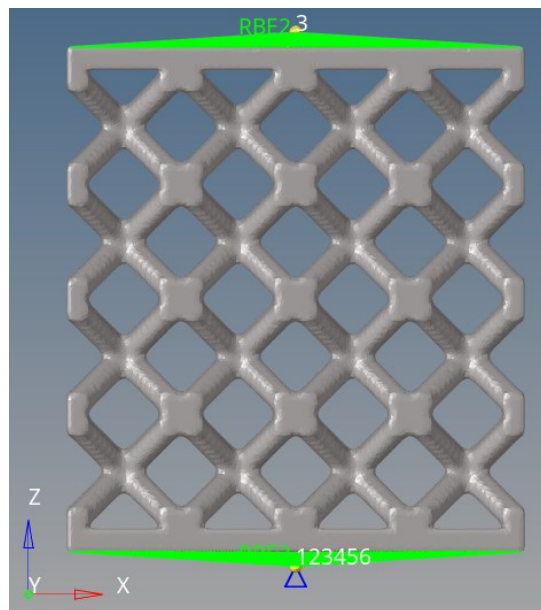


Figure 4.9. FEA boundary conditions of compression test specimen with BCC.

Graphs from Figure 4.10 to Figure 4.14 show the nominal stress-strain curves obtained from tension tests and their corresponding FEA results.

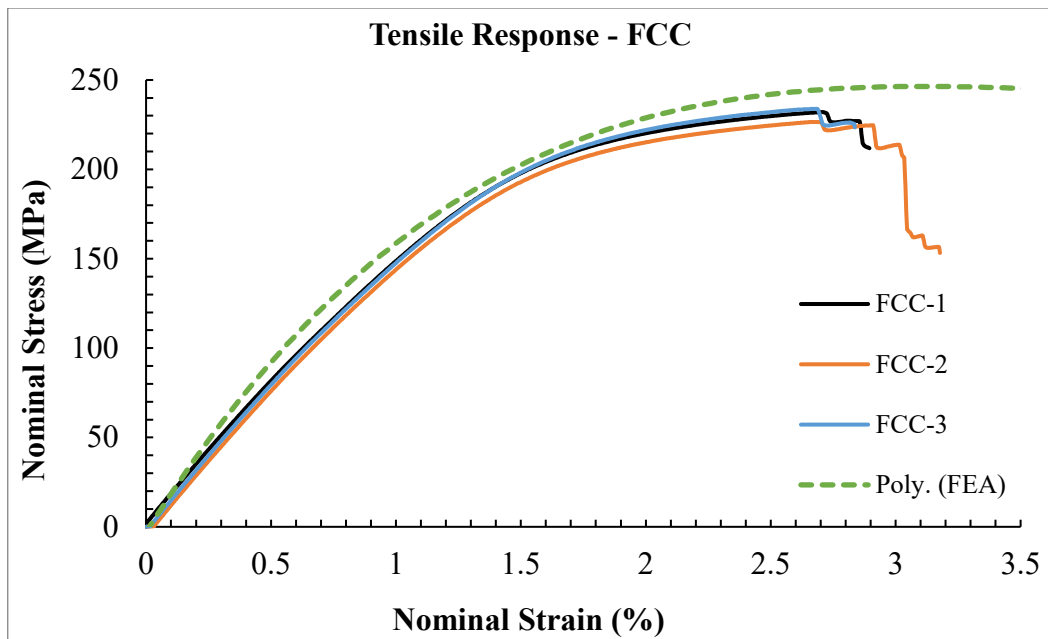


Figure 4.10. Comparison of FEA and experimental results of FCC under tensile loading.

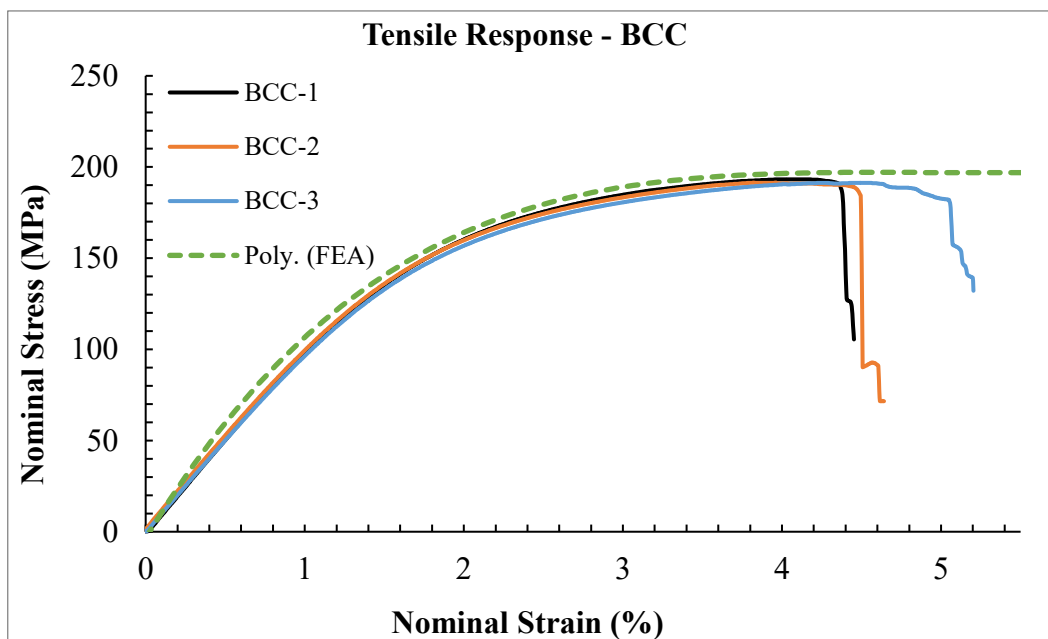


Figure 4.11. Comparison of FEA and experimental results of BCC under tensile loading.

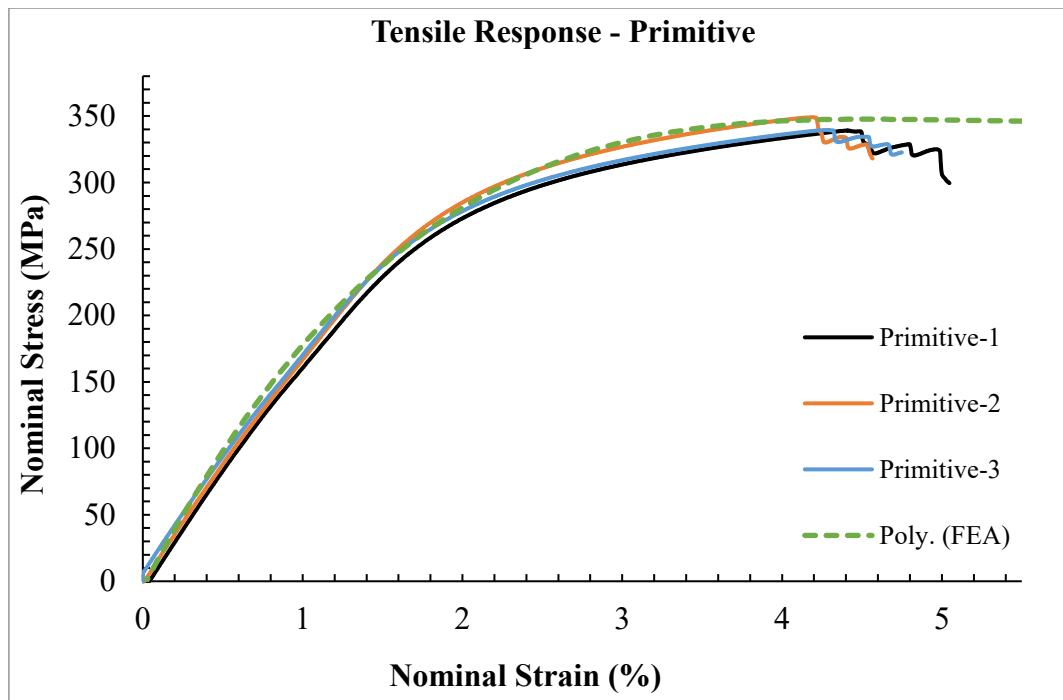


Figure 4.12. Comparison of FEA and experimental results of Primitive under tensile loading.

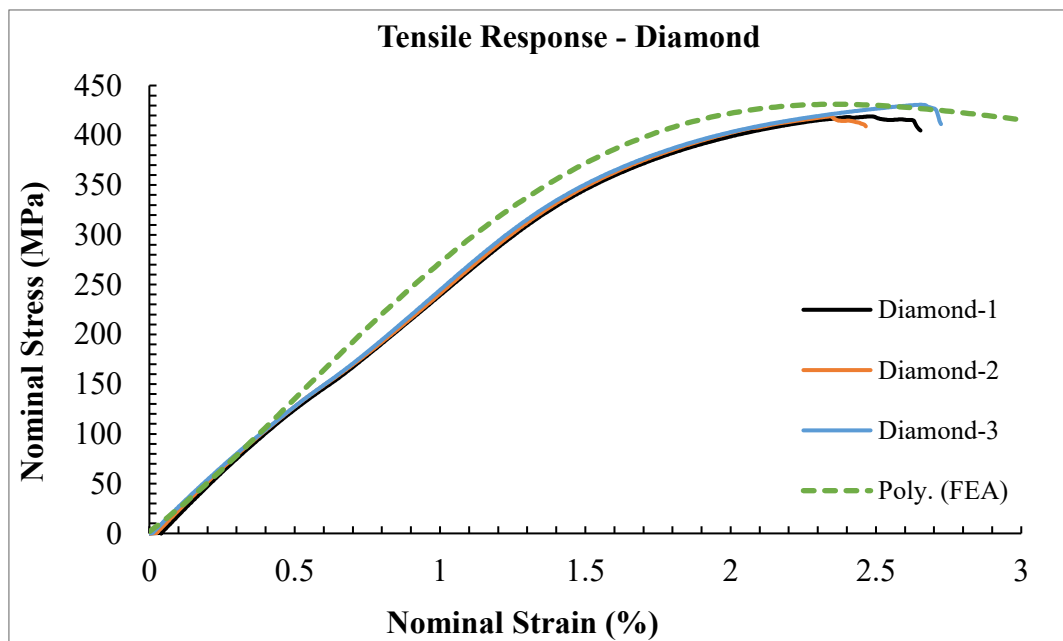


Figure 4.13. Comparison of FEA and experimental results of Diamond under tensile loading.

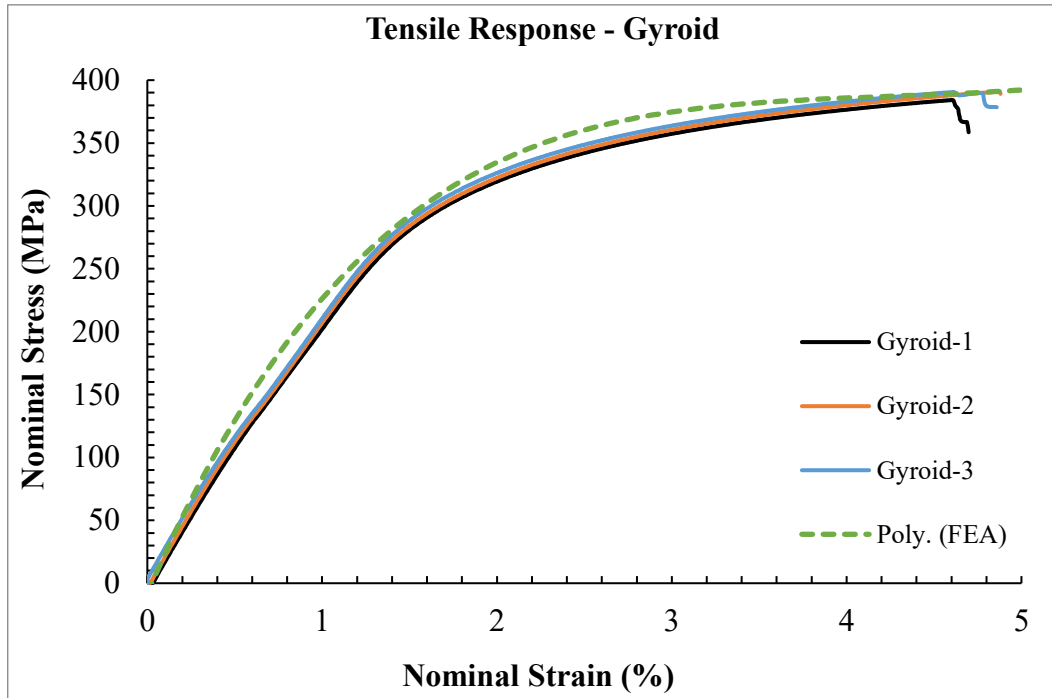


Figure 4.14. Comparison of FEA and experimental results of Gyroid under tensile loading.

It can be seen from presented figures that the test data and finite element results are compatible. It should be noted that the FEA performed under nonlinear static conditions with elastic modulus and yield strength values extracted from experiments. Therefore, the FEA data continue after fracture of real specimens which are not shown in given figures since there is no failure mode defined for tensile specimens due to convergence problem of small element sizes (0.2 mm on average).

Following images from Figure 4.15 to Figure 4.19 show the fracture regions of the tensile test specimens along with the von Mises stress distribution from FEA. While fracture occurs at nearly straight sections in other topologies, a 45° shear band is observed in the BCC geometry due to sequential failure in the strut joint regions where stress concentrations are accumulated, which is compatible to the similar results previously reported in the literature [75]. On the other hand, the absence of early refraction in the solid-lattice transition region in any of the pieces indicates that the thickness increase applied in this region provides successful results.

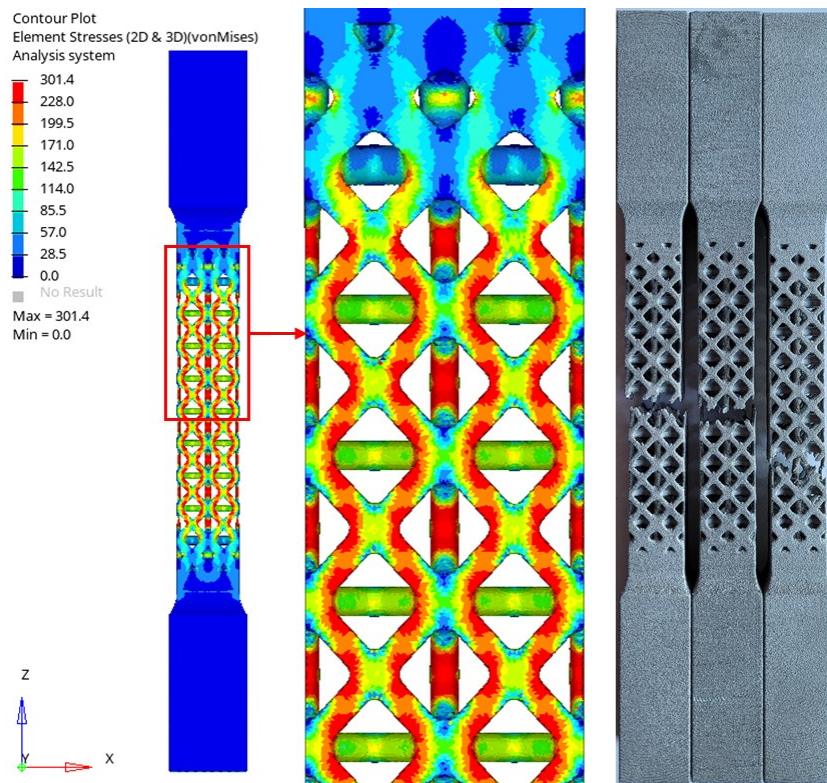


Figure 4.15. von Mises stress plot and fractured tension specimens of FCC.

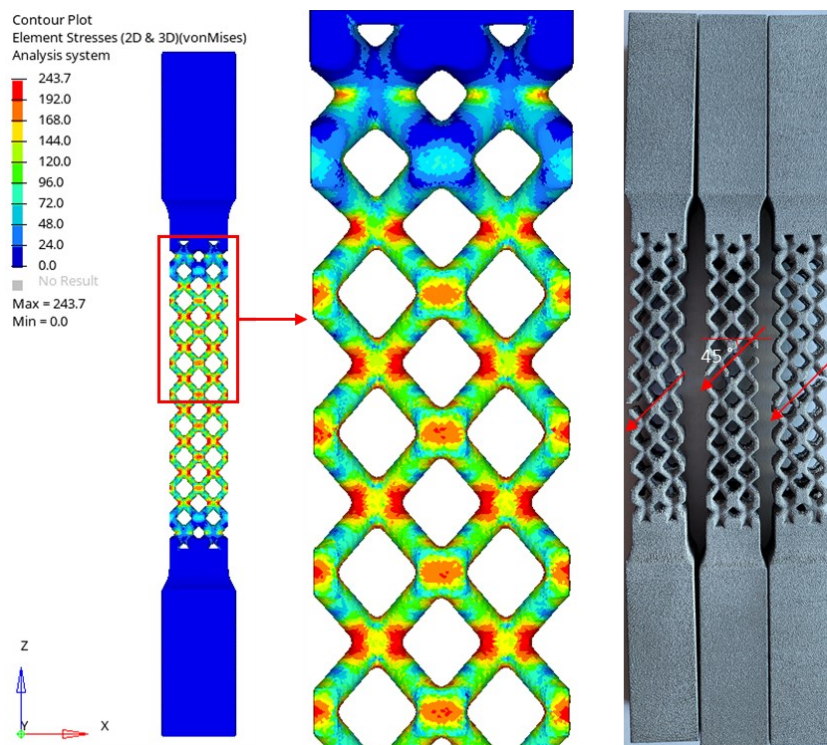


Figure 4.16. von Mises stress plot and fractured tension specimens of BCC.

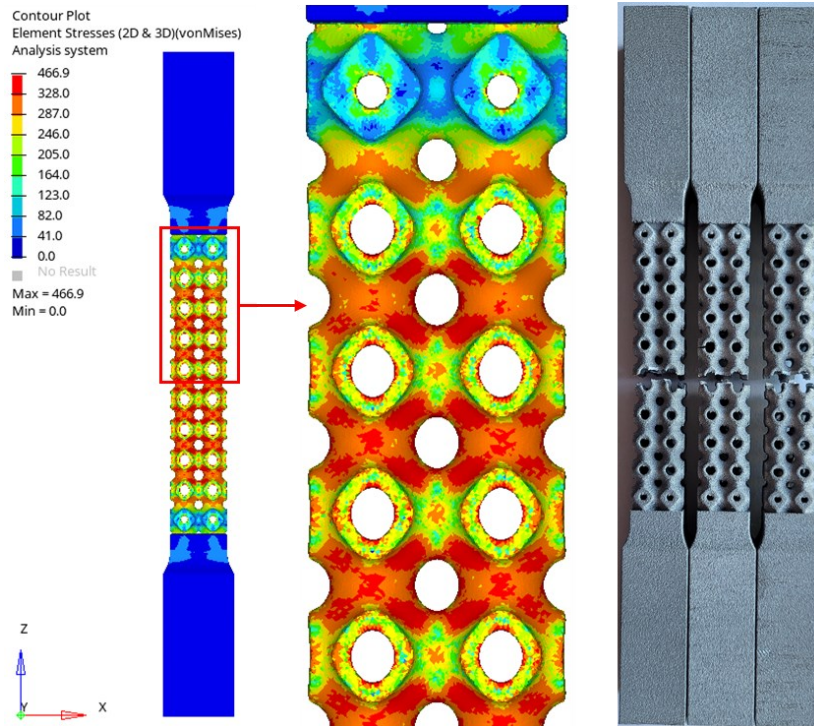


Figure 4.17. von Mises stress plot and fractured tension specimens of Primitive.

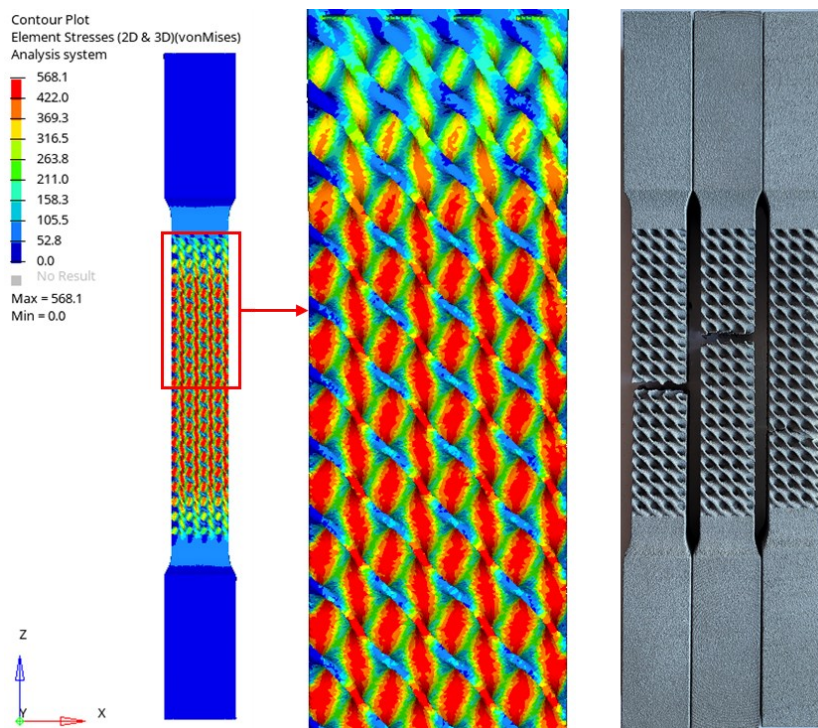


Figure 4.18. von Mises stress plot and fractured tension specimens of Diamond.

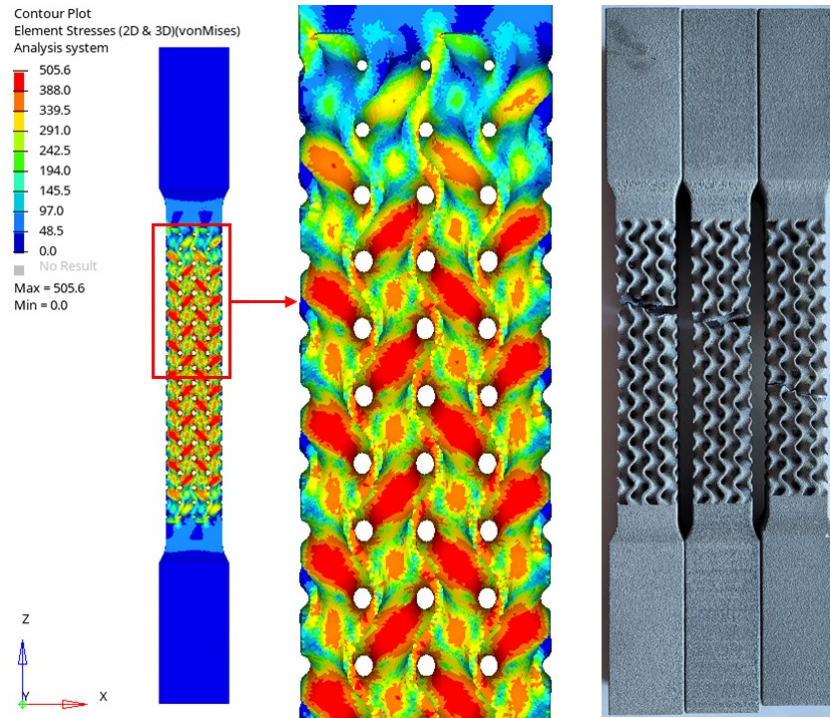


Figure 4.19. von Mises stress plot and fractured tension specimens of Gyroid.

It should be noted that the leftmost tensile specimen in Figure 4.16 has a bended-like appearance due to stopping of actuator head before all the unit cells break, caused by the large amount of drop in the loading. The similar situation is also experienced in the Gyroid and Diamond samples, so it is seen that the rightmost samples in Figure 4.18 and Figure 4.19 are not completely fractured.

In the FEA models of compression samples, since there is no verified data that provides the necessary coefficients for the definition of the damage mechanisms, analyses are carried out by loading up to 10% strain level which coincides that samples approach their first maximum compressive stress. Non-linear material curves obtained from the tests are defined to the models with the help of MATS1 card using total strain approach to examine the behavior after the yield point.

Graphs from Figure 4.20 to Figure 4.24 show the nominal stress-strain curves obtained from tension tests and their corresponding FEA results.

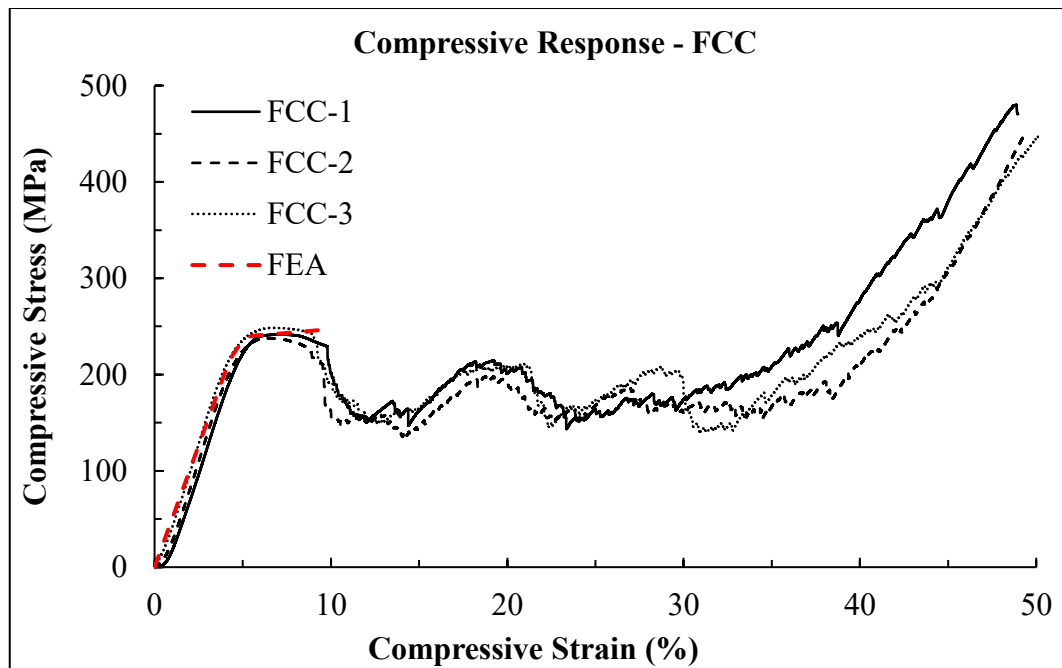


Figure 4.20. Comparison of FEA and experimental results of FCC under compressive loading.

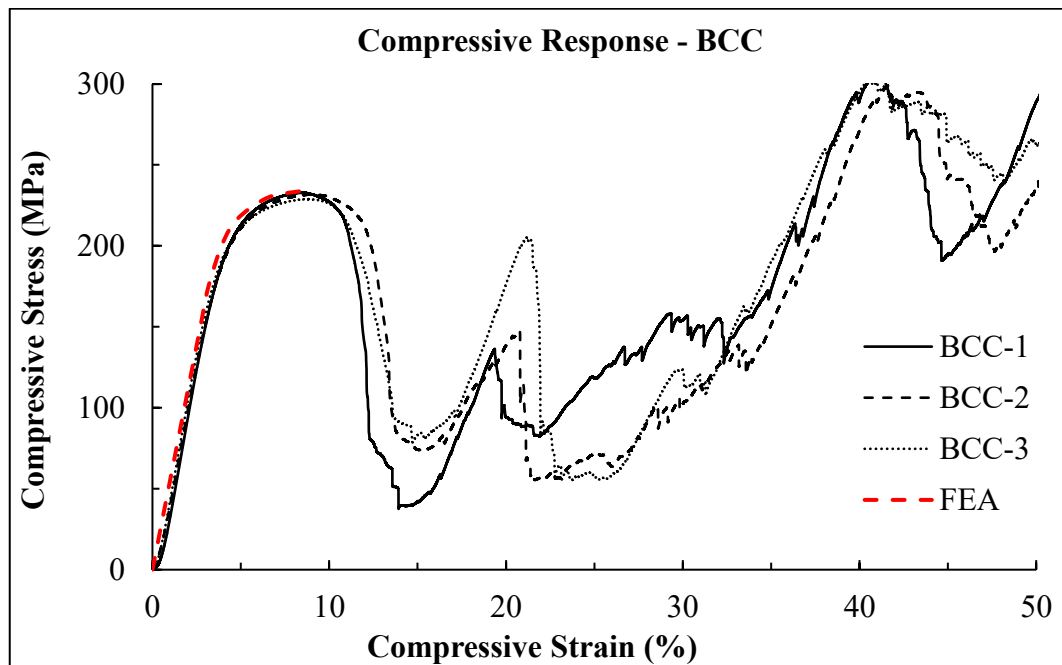


Figure 4.21. Comparison of FEA and experimental results of BCC under compressive loading.

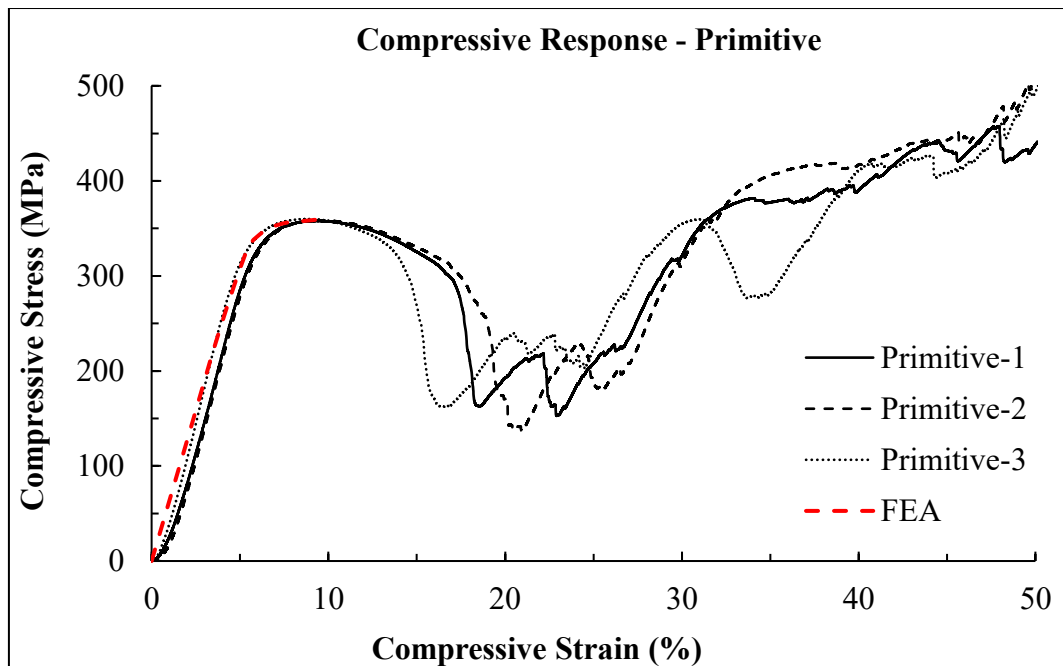


Figure 4.22. Comparison of FEA and experimental results of Primitive under compressive loading.

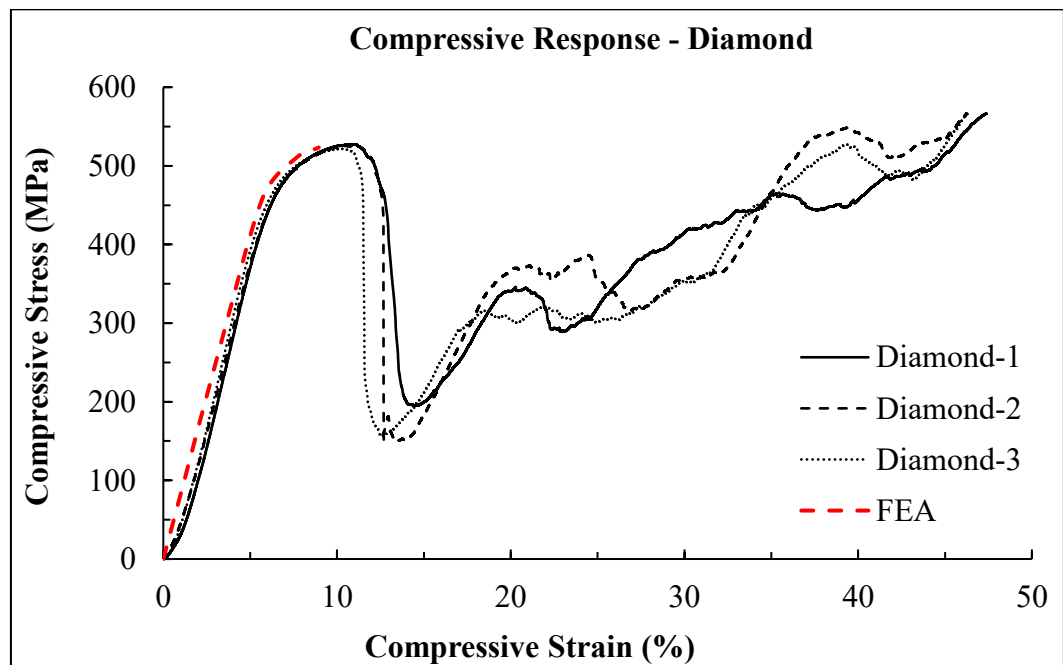


Figure 4.23. Comparison of FEA and experimental results of Diamond under compressive loading.

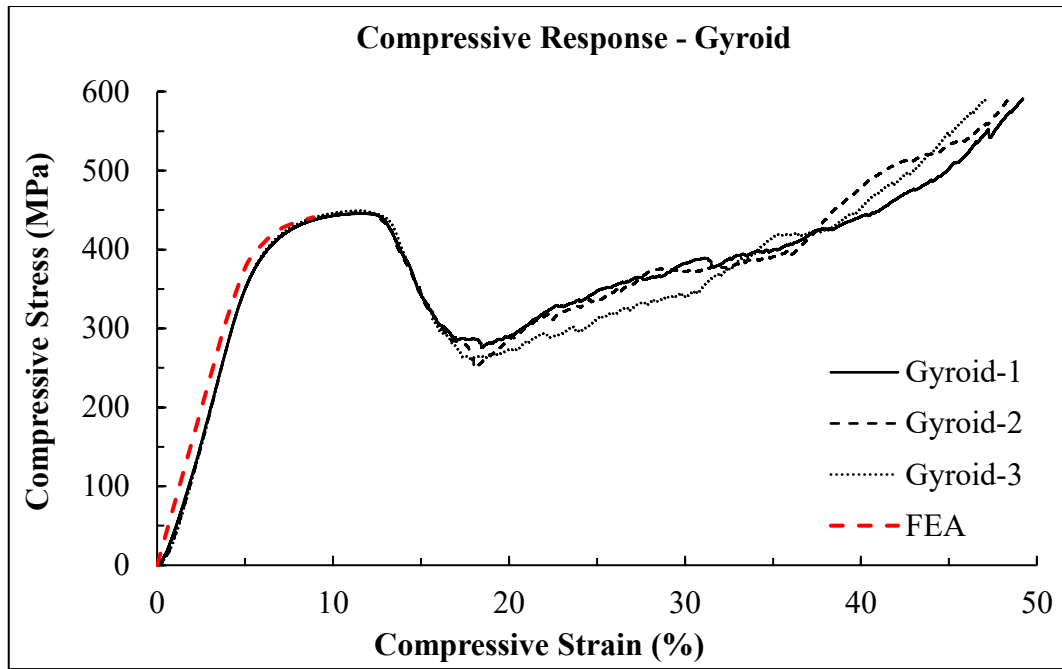


Figure 4.24. Comparison of FEA and experimental results of Gyroid under compressive loading.

It can be drawn from the graphs presented above that the finite element models and the experimental results are highly consistent up to first maximum compressive stress point for the compression samples. Due to the computational time considerations and convergence problems as well as the lack of reliable data for damage model parameters, analyses are limited to the region before first stress drop. On the other hand, the deformation and von Mises stress plots are provided in the following figures from Figure 4.25 to Figure 4.29. The barrel-like deformation at 10% compressive strain level observed in experiments can be clearly confirmed with the FEA deformation plots. Additionally, for the FCC topology, the stress concentrations at the strut joints on the side surfaces are found to exceed the first maximum compressive stress level, which coincides with the first failure region seen in Figure 4.6. This can be attributed to the lack of neighboring cell support on the outward-most cell struts, especially at first cell rows located in the load introduction. Besides, the smooth distribution of stress over the structure in all TPMS lattices are remarkably apparent, which is consistent with previously presented studies in the

literature [49] [72]. Finally, the stress concentration at the joints along the diagonal of the structure in the BCC topology and stress condensation on the Gyroid angled close to 45° can be considered as precursors to the shear band mechanism detected in the experiments.

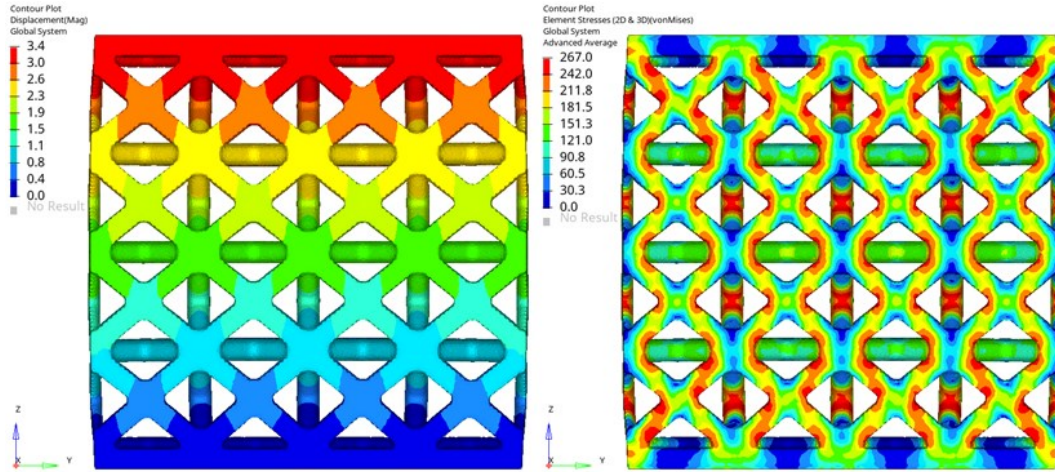


Figure 4.25. Displacement (left) and von Mises stress plots (right) for FCC at ~8% strain.

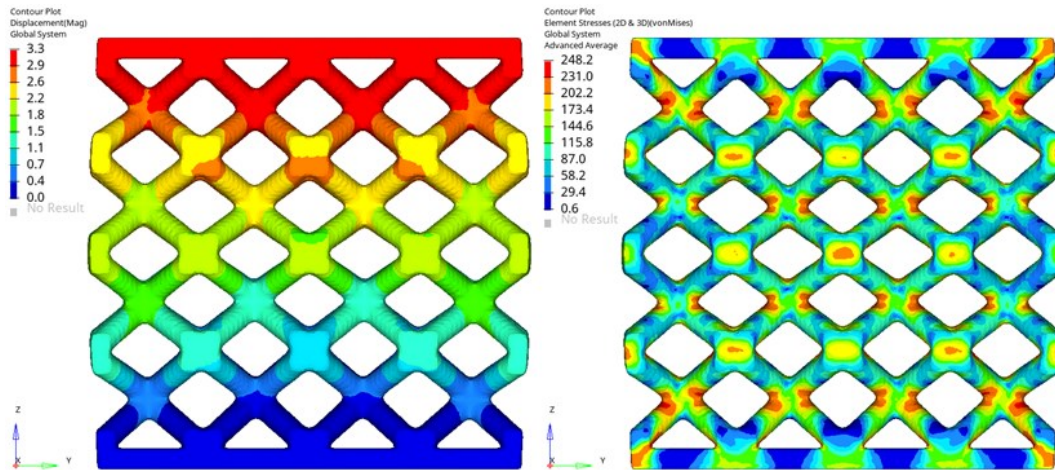


Figure 4.26. Displacement (left) and von Mises stress plots (right) for BCC at ~8% strain.

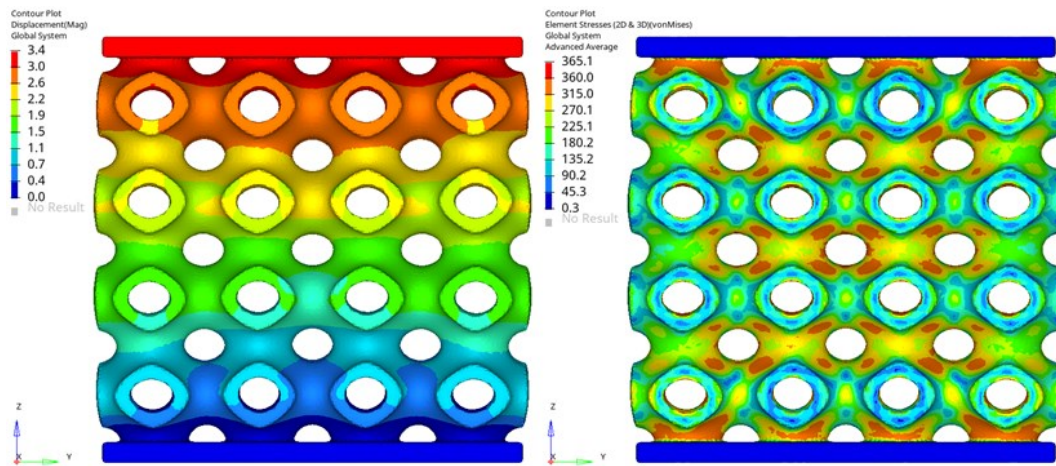


Figure 4.27. Displacement (left) and von Mises stress plots (right) for Primitive at ~8% strain.

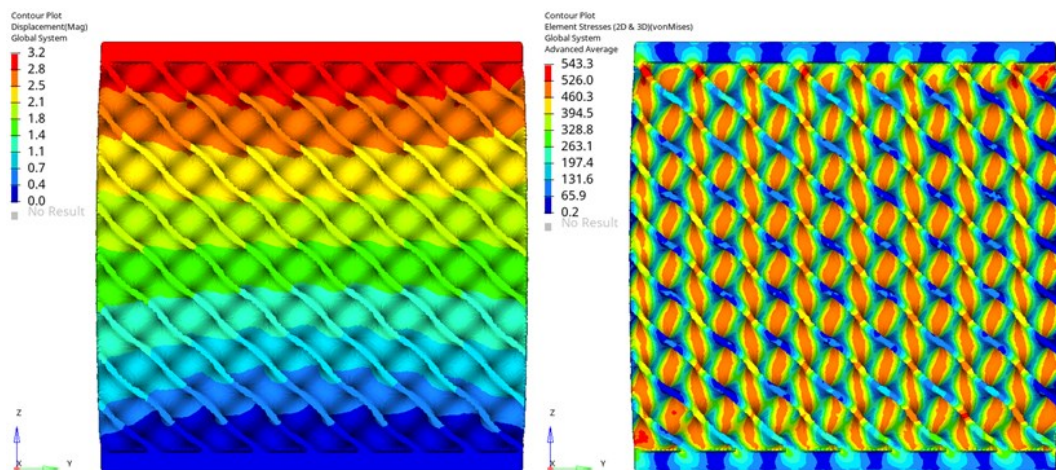


Figure 4.28. Displacement (left) and von Mises stress plots (right) for Diamond at ~8% strain.

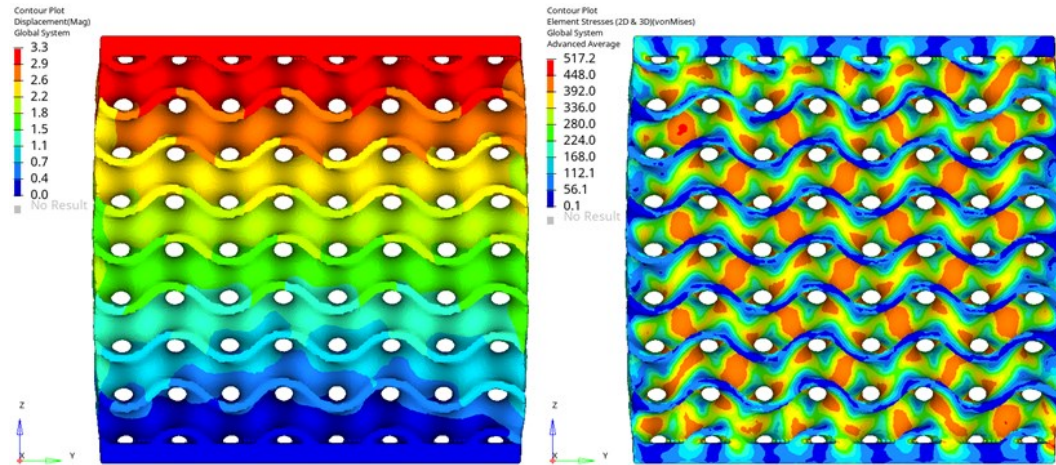


Figure 4.29. Displacement (left) and von Mises stress plots (right) for Gyroid at ~8% strain.

4.4 Microstructure Investigation

Mechanical properties of materials are directly related to their microstructure. Since the EBM method is carried out under elevated temperatures and existence of a melting-cooling cycle of the metals, the microstructures of parts and therefore their mechanical properties get affected depending on the process. Because the effect of different process parameters is eliminated in this study, the microstructure variations that may be related to the lattice topology and the location of the part on the build table are examined.

To investigate the microstructure, tensile test specimens of each lattice topology are cut in their transverse plane with respect to build direction. Extracted portions of the specimens are mounted in bakelite by using acrylic powder at Struers (Denmark) CitoPress-1 Mounting Press (see Figure 4.30). Following the mounting process, grinding is applied to parts with Silicon Carbide (SiC) abrasive in successive steps starting from coarse to fine. Polishing is done with Aluminum Oxide (Al_2O_3) after grinding. Both grinding and polishing operations are carried out by using Struers LaboForce-100 (see Figure 4.30). Etching process take place at the end of the process

by using Kroll's Reagent. The microstructures of prepared specimens are inspected on the CLEMEX (Canada) Nikon ECLIPSE MA100 (see Figure 4.31).



Figure 4.30. Struers CitoPress-1 Mounting Press (left) and Struers LaboForce-100 (right) machines.



Figure 4.31. Nikon ECLIPSE MA100 Optical Microscope.

Ti-6Al-4V alloy is the combination of a Vanadium-stabilized body-centered cubic beta phase and an Aluminum-stabilized hexagonal closed-packed alpha phase at room temperature, and its microstructure varies significantly depending on the thermal history. The captured microstructure images of all lattices are presented in Figure 4.32 where darker regions represents large prior-beta grains and lighter areas indicates the fine alpha phase within. The microstructures of all specimens having inhomogeneous although fine with basketweave formation and colony pattern of alpha-beta lamellae in equiaxed grains. Microstructures obtained in our study consistent with the cross-sectional images of vertically oriented samples in the work of Bass where microstructures of specimens in different orientations were examined [76]. Beyond the formation of microstructures, manufacturing defects e.g. porosities are observed in varying shapes and dimensions (marked in Figure 4.32). Apart from the occurrence of these pores are located generally at the near edge sites, the largest and highest in the amount of porosities are detected on the Gyroid topology.

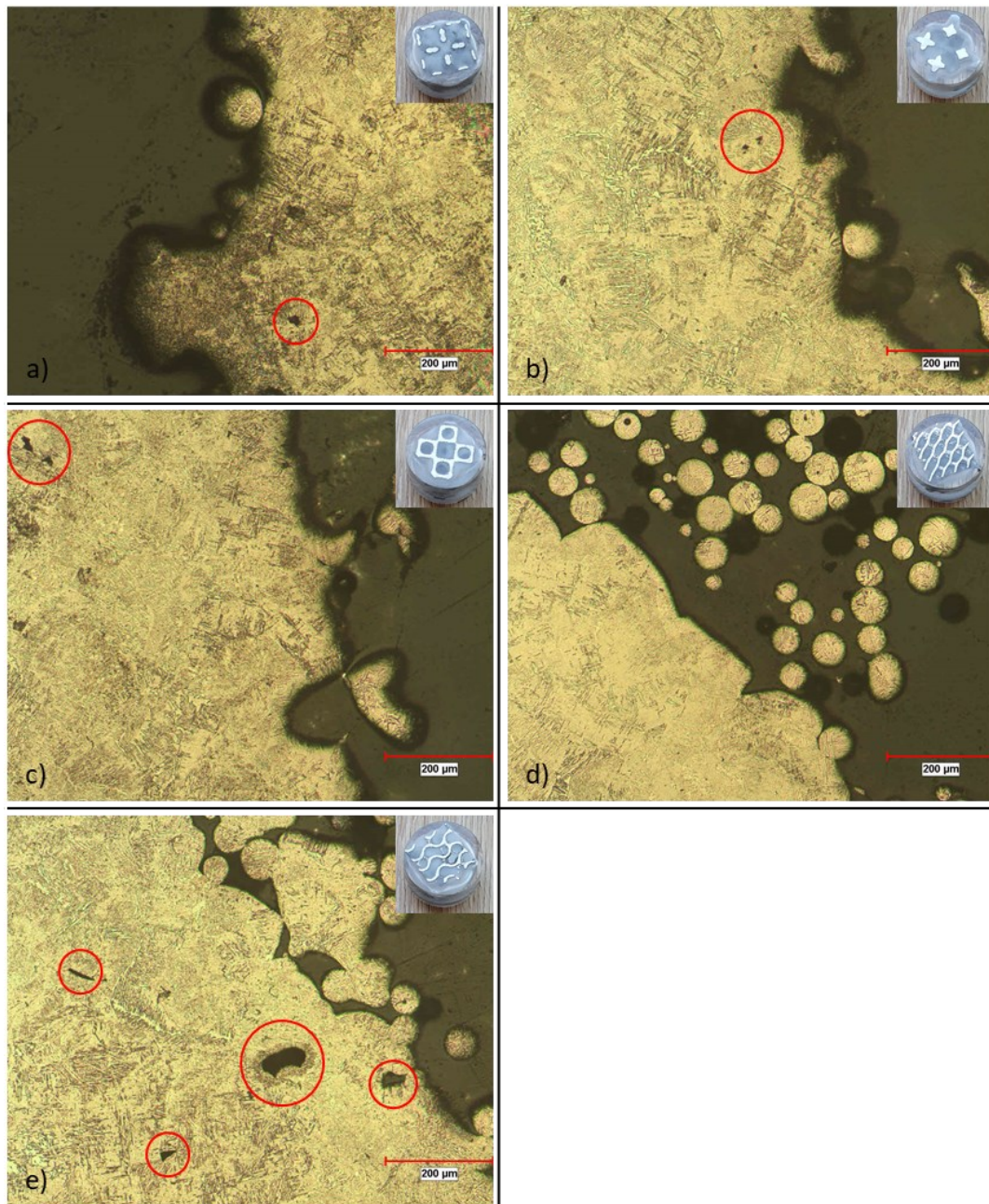


Figure 4.32. Microstructures of fractured tensile test specimen portions: a) FCC b) BCC c) Primitive d) Diamond e) Gyroid.

CHAPTER 5

CONCLUSION AND FUTURE WORK

This thesis work focused on the comparison of the mechanical properties of two strut-based (BCC and FCC) and three sheet-based TPMS (Primitive, Diamond and Gyroid) lattice structure topologies under compression and tension load conditions. Within the scope of the study, tensile and compression test specimens were produced in a single production batch by using EBM, three from each topology (30 specimens in total), applying the identical unit cell parameters and process parameter set. After powder removal and SEM investigations of the parts, tensile and compression tests were carried out. Finally, the fracture surfaces were examined. The following observations were drawn from the results:

- Sintering of unused powders is an important problem in lattice structures produced with EBM. Although several methods were tried in the literature such as chemical etching and ultrasound vibration following the standard PRS application, successful results could not be obtained. Similarly, in this study, manual powder removal was carried out by using a thin hand tool since PRS was insufficient. This means a very time-consuming post-process for lattice structures produced with EBM.
- In this study, produced samples are used in as-built state. SEM investigations revealed there is large amount of unmelted powders adhered to the melted surfaces. It is reported in the literature that these particles do not significantly affect the static behavior of parts, but may become critical for parts under cyclic loading. Furthermore, it is observed that the amount of unmelted particles adhered to the up-facing surfaces are relatively less than the down-facing surfaces.

- Tensile tests gave consistent and reproducible results for all three samples of all topologies. Thickness grading in the lattice-solid transition region successfully prevented the possibility of early fracture of lattices due to stress concentrations arise from sudden drop in the cross section. Tensile tests conducted with samples produced in the same batch with identical process parameters showed that TPMS lattices have approximately two times higher strength than strut-based lattices. Among all topologies, Diamond showed the highest UTS (422 MPa) with ~2.5% strain at the time of failure while BCC has the lowest UTS (192 MPa) at ~4.5% strain.
- The compressive mechanical properties showed consistent behavior until the first stress drop. However, they formed a plateau at different levels by showing varying fluctuations due to the manufacturing-related surface defects. Gyroid showed more smooth and stable deformation among all topologies, hence showed highest energy absorption capability by having 180.2 MJ/m³. On the other hand, the highest strength is seen in the Diamond again with 526 MPa first maximum compressive strength. Based on the results, strut-based topologies will be proper for weight reduction in areas where high stiffness is not required, and sheet-based TPMS lattices to be suitable for applications where load absorption and strength is important.
- According to the Gibson-Ashby model, the produced samples partially compliant with the dictated coefficient ranges, but the values slightly above the upper limit can be attributed to the margin of error seen in the density measurements and the trapped powder inside parts.
- Finite element results are compatible with the experimental results. The stress concentration regions with von Mises stress exceeding UTS and first maximum compressive stress levels are indicating the fracture sections of real specimens.

In the light of the problems and deficiencies encountered during this study, it is thought that it would be beneficial to carry out future studies in the following areas:

- Results obtained in this study are specific to the selected unit cell dimensions and volume fraction combination. Further studies focusing on the effect of varying unit cell dimensions for a fixed volume fraction might be useful.
- PRS process offered by Arcam is found as incapable of successfully remove semi-sintered powder from tight regions. It is necessary to develop new methods for powder removal from EBM products without the need for additional post-processing and without affecting the mechanical properties of the parts.
- Although the tensile and compression behaviors of the most common lattice structures in the literature were examined in this study, it would be useful to investigate the behavior of these topologies against combined load situations such as bending or shear forces that they possibly encounter during their service life.

REFERENCES

- [1] Hubs, “Additive manufacturing trend report 2021,” 2021.
- [2] SME, “Additive Manufacturing Glossary.”
<https://www.sme.org/technologies/additive-manufacturing-glossary/>
(accessed Nov. 20, 2021).
- [3] ISO/ASTM. (2016). *Standard Terminology for Additive Manufacturing – General Principles – Terminology* (ISO/ASTM Standard No. 52900:2015).
- [4] I. Gibson, D. Rosen, and B. Stucker, “Development of Additive Manufacturing Technology,” in *Additive Manufacturing Technologies*, 2nd ed., New York, NY: Springer, 2015, pp. 19–42. doi: 10.1007/978-1-4939-2113-3_2.
- [5] I. Gibson, D. Rosen, and B. Stucker, “Powder Bed Fusion Processes,” in *Additive Manufacturing Technologies*, 2nd ed., New York, NY: Springer, 2015, pp. 107–145. doi: 10.1007/978-1-4939-2113-3_5.
- [6] R. Wauthle *et al.*, “Effects of build orientation and heat treatment on the microstructure and mechanical properties of selective laser melted Ti6Al4V lattice structures,” *Additive Manufacturing*, vol. 5, pp. 77–84, Jan. 2015, doi: 10.1016/J.ADDMA.2014.12.008.
- [7] G. W. Kooistra, V. S. Deshpande, and H. N. G. Wadley, “Compressive behavior of age hardenable tetrahedral lattice truss structures made from aluminium,” *Acta Materialia*, vol. 52, no. 14, pp. 4229–4237, 2004, doi: 10.1016/j.actamat.2004.05.039.
- [8] H. N. G. Wadley, N. A. Fleck, and A. G. Evans, “Fabrication and structural performance of periodic cellular metal sandwich structures,” *Composites Science and Technology*, vol. 63, no. 16, pp. 2331–2343, 2003, doi: 10.1016/S0266-3538(03)00266-5.

- [9] F. Hualin *et al.*, “Design and Manufacturing of a Composite Lattice Structure Reinforced by Continuous Carbon Fibers,” 2006.
- [10] A. D. Voicu, A. Hadăr, and D. Vlăsceanu, “Benefits of 3D printing technologies for aerospace lattice structures,” *Scientific Bulletin of Naval Academy*, vol. 24, no. 1, pp. 8–16, 2021, doi: 10.21279/1454-864X-21-I1-001.
- [11] V. Kumar, G. Manogharan, and D. R. Cormier, “Design of periodic cellular structures for heat exchanger applications,” *20th Annual International Solid Freeform Fabrication Symposium, SFF 2009*, pp. 738–748, 2009.
- [12] D. Downing, M. Leary, M. McMillan, A. Alghamdi, and M. Brandt, “Heat transfer in lattice structures during metal additive manufacturing: numerical exploration of temperature field evolution,” *Rapid Prototyping Journal*, vol. 26, no. 5, pp. 911–928, May 2020, doi: 10.1108/RPJ-11-2018-0288.
- [13] Y. Xiong *et al.*, “Fatigue behavior and osseointegration of porous Ti-6Al-4V scaffolds with dense core for dental application,” *Materials and Design*, vol. 195, p. 108994, 2020, doi: 10.1016/j.matdes.2020.108994.
- [14] L. J. Gibson and M. F. Ashby, *Cellular Solids: Structure and Properties*, vol. 2, no. 4. 1997. doi: 10.1017/CBO9781139878326.004.
- [15] M. F. Ashby, “The properties of foams and lattices,” *Phil. Trans. R. Soc. A.*, vol. 364, pp. 15–30, 2006, doi: 10.1098/rsta.2005.1678.
- [16] A. G. Evans, J. W. Hutchinson, and M. F. Ashby, “Multifunctionality of cellular metal systems,” *Progress in Materials Science*, vol. 43, no. 3, pp. 171–221, 1998, doi: 10.1016/S0079-6425(98)00004-8.
- [17] G. Dong, Y. Tang, and Y. F. Zhao, “A survey of modeling of lattice structures fabricated by additive manufacturing,” *Journal of Mechanical Design, Transactions of the ASME*, vol. 139, no. 10, Oct. 2017, doi: 10.1115/1.4037305.

- [18] W. Tao and M. C. Leu, “Design of lattice structure for additive manufacturing,” in *International Symposium on Flexible Automation, ISFA 2016*, Dec. 2016, pp. 325–332. doi: 10.1109/ISFA.2016.7790182.
- [19] J. R. Hook and H. E. Hall, “Crystal structure,” in *Solid State Physics*, 2nd ed., Chichester, West Sussex: John Wiley & Sons, 1991, pp. 18–47.
- [20] P. J. F. Gandy, D. Cvijovic, A. L. Mackay, and J. Klinowski, “Exact computation of the triply periodic D (‘diamond’) minimal surface,” *Chemical Physics Letters*, vol. 314, pp. 543–551, 1999.
- [21] H. Jia *et al.*, “An experimental and numerical investigation of compressive response of designed Schwarz Primitive triply periodic minimal surface with non-uniform shell thickness,” *Extreme Mech Lett*, vol. 37, May 2020, doi: 10.1016/j.eml.2020.100671.
- [22] D.-Jin. Yoo, “Advanced porous scaffold design using multi-void triply periodic minimal surface models with high surface area to volume ratios,” *International Journal of Precision Engineering and Manufacturing*, vol. 15, no. 8, pp. 1657–1666, 2014, doi: 10.1007/s12541-014-0516-5.
- [23] E. H. Khogalia, H. L. Choo, and W. H. Yap, “Performance of triply periodic minimal surface lattice structures under compressive loading for tissue engineering applications,” in *AIP Conference Proceedings*, May 2020, vol. 2233. doi: 10.1063/5.0001631.
- [24] I. Maskery *et al.*, “Insights into the mechanical properties of several triply periodic minimal surface lattice structures made by polymer additive manufacturing,” *Polymer*, vol. 152, pp. 62–71, Sep. 2018, doi: 10.1016/j.polymer.2017.11.049.
- [25] H. Karcher and K. Polthier, “Construction of Triply Periodic Minimal Surfaces,” 1996.

- [26] J. Shin *et al.*, “Finite element analysis of Schwarz P surface pore geometries for tissue-engineered scaffolds,” *Mathematical Problems in Engineering*, vol. 2012, 2012, doi: 10.1155/2012/694194.
- [27] A. H. Schoen, “Infinite periodic minimal surfaces without self-intersections,” *Nasa Technical Note D-5541*, p. 92, 1970.
- [28] J. C. Maxwell, “L. On the calculation of the equilibrium and stiffness of frames,” *The London, Edinburgh, and Dublin Philosophical Magazine and Journal of Science*, vol. 27, pp. 294–299, 1864.
- [29] C. R. Calladine, “Purely ‘equilibrium’ solutions for shells: the membrane hypothesis,” in *Theory of shell structures*, New York, NY: Cambridge University Press, 1983, pp. 80–123.
- [30] V. S. Deshpande, N. A. Fleck, and M. F. Ashby, “Effective properties of the octet-truss lattice material,” *Journal of the Mechanics and Physics of Solids*, vol. 49, no. 8, pp. 1747–1769, Aug. 2001, doi: 10.1016/S0022-5096(01)00010-2.
- [31] M. Mazur, M. Leary, M. McMillan, S. Sun, D. Shidid, and M. Brandt, “Mechanical properties of Ti6Al4V and AlSi12Mg lattice structures manufactured by Selective Laser Melting (SLM),” *Laser Additive Manufacturing: Materials, Design, Technologies, and Applications*, pp. 119–161, Jan. 2017, doi: 10.1016/B978-0-08-100433-3.00005-1.
- [32] H. D. Carlton *et al.*, “Mapping local deformation behavior in single cell metal lattice structures,” *Acta Materialia*, vol. 129, pp. 239–250, May 2017, doi: 10.1016/j.actamat.2017.02.023.
- [33] S. J. Li *et al.*, “Influence of cell shape on mechanical properties of Ti–6Al–4V meshes fabricated by electron beam melting method,” *Acta Biomaterialia*, vol. 10, no. 10, pp. 4537–4547, Oct. 2014, doi: 10.1016/j.actbio.2014.06.010.

- [34] I. Maskery, N. T. Aboulkhair, A. O. Aremu, C. J. Tuck, and I. A. Ashcroft, “Compressive failure modes and energy absorption in additively manufactured double gyroid lattices,” *Additive Manufacturing*, vol. 16, pp. 24–29, Aug. 2017, doi: 10.1016/J.ADDMA.2017.04.003.
- [35] J. Kadkhodapour *et al.*, “Failure mechanisms of additively manufactured porous biomaterials: Effects of porosity and type of unit cell,” *Journal of the Mechanical Behavior of Biomedical Materials*, vol. 50, pp. 180–191, Oct. 2015, doi: 10.1016/J.JMBBM.2015.06.012.
- [36] N. Vanderesse, A. Richter, N. Nuño, and P. Bocher, “Measurement of deformation heterogeneities in additive manufactured lattice materials by Digital Image Correlation: Strain maps analysis and reliability assessment,” *Journal of the Mechanical Behavior of Biomedical Materials*, vol. 86, pp. 397–408, Oct. 2018, doi: 10.1016/J.JMBBM.2018.07.010.
- [37] E. Alabort, D. Barba, and R. C. Reed, “Design of metallic bone by additive manufacturing,” *Scripta Materialia*, vol. 164, pp. 110–114, Apr. 2019, doi: 10.1016/J.SCRIPTAMAT.2019.01.022.
- [38] P. Hanzl, I. Zetková, and M. Daňa, “Uniaxial Tensile Load of Lattice Structures Produced by Metal Additive Manufacturing,” *Manufacturing Technology*, vol. 19, no. 2, pp. 228–231, 2019, doi: 10.21062/ujep/274.2019/a/1213-2489/MT/19/2/228.
- [39] S. Y. Park, K. S. Kim, B. AlMangour, D. Grzesiak, and K. A. Lee, “Effect of unit cell topology on the tensile loading responses of additive manufactured CoCrMo triply periodic minimal surface sheet lattices,” *Materials & Design*, vol. 206, p. 109778, Aug. 2021, doi: 10.1016/J.MATDES.2021.109778.
- [40] O. Rehme and C. Emmelmann, “Rapid manufacturing of lattice structures with selective laser melting,” in *Proc. SPIE 6107, Laser-based Micropackaging*, Feb. 2006, vol. 6107. doi: 10.1117/12.645848.

- [41] S. McKown *et al.*, “The quasi-static and blast loading response of lattice structures,” *International Journal of Impact Engineering*, vol. 35, no. 8, pp. 795–810, Aug. 2008, doi: 10.1016/J.IJIMPENG.2007.10.005.
- [42] Z. Xiao, Y. Yang, R. Xiao, Y. Bai, C. Song, and D. Wang, “Evaluation of topology-optimized lattice structures manufactured via selective laser melting,” *Materials & Design*, vol. 143, pp. 27–37, Apr. 2018, doi: 10.1016/J.MATDES.2018.01.023.
- [43] C. Peng, P. Tran, H. Nguyen-Xuan, and A. J. M. Ferreira, “Mechanical performance and fatigue life prediction of lattice structures: Parametric computational approach,” *Composite Structures*, vol. 235, p. 111821, Mar. 2020, doi: 10.1016/J.COMPSTRUCT.2019.111821.
- [44] R. Guo *et al.*, “Numerical Analysis on Static Mechanical Properties of the Periodic Multilayer Lattice Material,” *Engineering*, vol. 3, no. 12, pp. 1149–1154, 2011, doi: 10.4236/eng.2011.312143.
- [45] S. Restrepo, S. Ocampo, J. A. Ramírez, C. Paucar, and C. García, “Mechanical properties of ceramic structures based on Triply Periodic Minimal Surface (TPMS) processed by 3D printing,” in *Journal of Physics: Conference Series*, 2017, vol. 935. doi: 10.1088/1742-6596/935/1/012036.
- [46] D. Khrapov *et al.*, “Different Approaches for Manufacturing Ti-6Al-4V Alloy with Triply Periodic Minimal Surface Sheet-Based Structures by Electron Beam Melting,” *Materials*, vol. 14, no. 17, Sep. 2021, doi: 10.3390/ma14174912.
- [47] H. Hasib, “Mechanical Behavior of Non-Stochastic Ti-6Al-4V Cellular Structures Produced via Electron Beam Melting (EBM),” Raleigh, North Carolina, 2011.
- [48] M. Jamshidinia, L. Wang, W. Tong, and R. Kovacevic, “The bio-compatible dental implant designed by using non-stochastic porosity produced by Electron Beam Melting (EBM),” *Journal of Materials Processing*

- Technology*, vol. 214, no. 8, pp. 1728–1739, Aug. 2014, doi: 10.1016/J.JMATPROTEC.2014.02.025.
- [49] L. Zhang *et al.*, “Energy absorption characteristics of metallic triply periodic minimal surface sheet structures under compressive loading,” *Additive Manufacturing*, vol. 23, pp. 505–515, Oct. 2018, doi: 10.1016/J.ADDMA.2018.08.007.
- [50] S. M. Ahmadi *et al.*, “Additively Manufactured Open-Cell Porous Biomaterials Made from Six Different Space-Filling Unit Cells: The Mechanical and Morphological Properties,” *Materials*, vol. 8, pp. 1871–1896, 2015, doi: 10.3390/ma8041871.
- [51] T. Zhong, K. He, H. Li, and L. Yang, “Mechanical properties of lightweight 316L stainless steel lattice structures fabricated by selective laser melting,” *Materials & Design*, vol. 181, p. 108076, Nov. 2019, doi: 10.1016/J.MATDES.2019.108076.
- [52] GE, “Arcam EBM Q20plus.” <https://www.ge.com/additive/additive-manufacturing/machines/ebm-machines/arcam-ebm-q20plus> (accessed Dec. 17, 2021).
- [53] I. Maskery, A. O. Aremu, L. Parry, R. D. Wildman, C. J. Tuck, and I. A. Ashcroft, “Effective design and simulation of surface-based lattice structures featuring volume fraction and cell type grading,” *Materials and Design*, vol. 155, pp. 220–232, Oct. 2018, doi: 10.1016/j.matdes.2018.05.058.
- [54] O. Al-Ketan, R. Rowshan, and R. K. Abu Al-Rub, “Topology-mechanical property relationship of 3D printed strut, skeletal, and sheet based- periodic metallic cellular materials,” *Additive Manufacturing*, vol. 19, pp. 167–183, Jan. 2018, doi: 10.1016/j.addma.2017.12.006.
- [55] H. Alsalla, L. Hao, and C. Smith, “Fracture toughness and tensile strength of 316L stainless steel cellular lattice structures manufactured using the selective laser melting technique,” *Materials Science and Engineering: A*, vol. 669, pp. 1–6, Jul. 2016, doi: 10.1016/J.MSEA.2016.05.075.

- [56] ASTM Standard F3302-18. 2018. “Standard for Additive Manufacturing – Finished Part Properties – Standard Specification for Titanium Alloys via Powder Bed Fusion”. ASTM International. DOI: 10.1520/F3302-18

- [57] I. Maskery *et al.*, “Mechanical Properties of Ti-6Al-4V Selectively Laser Melted Parts with Body-Centred-Cubic Lattices of Varying cell size,” *Experimental Mechanics*, vol. 55, pp. 1261–1272, 2015, doi: 10.1007/s11340-015-0021-5.

- [58] ASTM Standard E8/E8M. 2010. “Standard Test Methods for Tension Testing of Metallic Materials”. ASTM International. DOI: 10.1520/E0008_E0008M-16AE01.

- [59] International Organization for Standardization. (2011). *Mechanical testing of metals - Ductility testing - Compression test for porous and cellular metals* (ISO Standard No. 13314:2011)

- [60] W. Ameen, A. Al-Ahmari, and O. Abdulhameed, “Design for Metal Additive Manufacturing: An Investigation of Key Design Application on Electron Beam Melting,” *World Academy of Science, Engineering and Technology, International Journal of Industrial and Manufacturing Engineering*, vol. 13, no. 4, pp. 265–269, 2019.

- [61] S. Wright, “Machine Guides - Arcam EBM Guide.md.” <https://github.com/Gongkai-AM/Machine-Guides/blob/master/Arcam%20EBM%20Guide.md> (accessed Dec. 25, 2021).

- [62] M. Suard, “Characterization and Optimization of Lattice Structures made by Electron Beam Melting,” no. November 2015, 2015.

- [63] D. Khrapov *et al.*, “The impact of post manufacturing treatment of functionally graded Ti6Al4V scaffolds on their surface morphology and mechanical strength,” *Journal of Materials Research and Technology*, vol. 9, no. 2, pp. 1866–1881, Mar. 2020, doi: 10.1016/J.JMRT.2019.12.019.

- [64] H. Hasib, O. L. Harrysson, and H. A. West, "Powder Removal from Ti-6Al-4V Cellular Structures Fabricated via Electron Beam Melting," *JOM*, vol. 67, no. 3, pp. 639–646, Mar. 2015, doi: 10.1007/s11837-015-1307-x.
- [65] P. Drescher, T. Reimann, and H. Seitz, "Investigation of powder removal of net-structured titanium parts made from electron beam melting," 2014.
- [66] S. Drücker, S. Inman, and B. Fiedler, "Simulation and Optimization of the Load Introduction Geometry of Additively Manufactured Lattice Structure Specimens," 2018.
- [67] J. Bruno, A. Rochman, and G. Cassar, "Effect of Build Orientation of Electron Beam Melting on Microstructure and Mechanical Properties of Ti-6Al-4V," *Journal of Materials Engineering and Performance*, vol. 26, no. 2, pp. 692–703, Feb. 2017, doi: 10.1007/s11665-017-2502-4.
- [68] F. Memu, "Katmanlı İmalat Yöntemiyle Üretilmiş Ti-6Al-4V Alaşımının Mekanik Özelliklerinin İncelenmesi," 2019.
- [69] G. Seiffert, C. Hopkins, and C. Sutcliffe, "Comparison of high-intensity sound and mechanical vibration for cleaning porous titanium cylinders fabricated using selective laser melting," *J Biomed Mater Res B Appl Biomater*, vol. 105, no. 1, pp. 117–123, 2017, doi: 10.1002/jbm.b.33535.
- [70] K. S. Chan, M. Koike, R. L. Mason, and T. Okabe, "Fatigue Life of Titanium Alloys Fabricated by Additive Layer Manufacturing Techniques for Dental Implants," *Metall Mater Trans A*, vol. 44, pp. 1010–1022, 2013, doi: 10.1007/s11661-012-1470-4.
- [71] X. Li *et al.*, "Investigation of Compressive and Tensile Behavior of Stainless Steel/Dissolvable Aluminum Bimetallic Composites by Finite Element Modeling and Digital Image Correlation," *Materials*, vol. 14, no. 13, 2021, doi: 10.3390/ma14133654.

- [72] Q. Sun, J. Sun, K. Guo, and L. Wang, “Compressive mechanical properties and energy absorption characteristics of SLM fabricated Ti6Al4V triply periodic minimal surface cellular structures,” *Mechanics of Materials*, vol. 166, p. 104241, Mar. 2022, doi: 10.1016/J.MECHMAT.2022.104241.
- [73] A. F. Obaton *et al.*, “Investigation of new volumetric non-destructive techniques to characterise additive manufacturing parts,” *Welding in the World*, vol. 62, no. 5, pp. 1049–1057, Sep. 2018, doi: 10.1007/S40194-018-0593-7.
- [74] T. Maconachie *et al.*, “SLM lattice structures: Properties, performance, applications and challenges,” *Materials and Design*, vol. 183, p. 108137, 2019, doi: 10.1016/j.matdes.2019.108137.
- [75] X. Liu, T. Wada, A. Suzuki, N. Takata, M. Kobashi, and M. Kato, “Understanding and suppressing shear band formation in strut-based lattice structures manufactured by laser powder bed fusion,” *Materials & Design*, vol. 199, p. 109416, Feb. 2021, doi: 10.1016/J.MATDES.2020.109416.
- [76] B. S. Bass, “Validating the Arcam EBM Process as an Alternative Fabrication Method for Titanium-6Al-4V Alloys,” Raleigh, 2010.